AFRL-AFOSR-VA-TR-2019-0347

Single Sheet Lasers for Attojoule Optoelectronics

Weidong Zhou
UNIVERSITY OF TEXAS AT ARLINGTON

02/28/2019
Final Report

Air Force Research Laboratory
AF Office Of Scientific Research (AFOSR)/ RTB1
Arlington, Virginia 22203
Air Force Materiel Command

DISTRIBUTION A: Distribution approved for public release.

REPORT DOCUMENTATION PAGE

Form Approved
OMB No. 0704-0188

1. REPORT DATE *(DD-MM-YYYY)*	2. REPORT TYPE	3. DATES COVERED *(From - To)*
15-11-2019	Final Performance	01 Dec 2015 to 30 Nov 2018

4. TITLE AND SUBTITLE
Single Sheet Lasers for Attojoule Optoelectronics

5a. CONTRACT NUMBER

5b. GRANT NUMBER
FA9550-16-1-0010

5c. PROGRAM ELEMENT NUMBER
61102F

6. AUTHOR(S)
Weidong Zhou, Shanhui Fan, Xiuling Li

5d. PROJECT NUMBER

5e. TASK NUMBER

5f. WORK UNIT NUMBER

7. PERFORMING ORGANIZATION NAME(S) AND ADDRESS(ES)
UNIVERSITY OF TEXAS AT ARLINGTON
1 UNIVERSITY OF TEXAS AT ARL
ARLINGTON, TX 76019-0001 US

8. PERFORMING ORGANIZATION REPORT NUMBER

9. SPONSORING/MONITORING AGENCY NAME(S) AND ADDRESS(ES)
AF Office of Scientific Research
875 N. Randolph St. Room 3112
Arlington, VA 22203

10. SPONSOR/MONITOR'S ACRONYM(S)
AFRL/AFOSR RTB1

11. SPONSOR/MONITOR'S REPORT NUMBER(S)
AFRL-AFOSR-VA-TR-2019-0347

12. DISTRIBUTION/AVAILABILITY STATEMENT
A DISTRIBUTION UNLIMITED: PB Public Release

13. SUPPLEMENTARY NOTES

14. ABSTRACT
The objective of this project is investigate laser scaling towards extreme energy efficiency. A range of photonic crystal cavities were proposed and investigated. Optically pumped room temperature lasers were achieved with low lasing threshold and high directional beam, based both on exfoliated and large area CVD WS2 materials on heterostructure photonic crystal cavities. Detailed investigations were carried out on the laser cavities and lasing characteristics, including spectral outputs, polarization, optical beam divergence angle, and lifetime measurements.

15. SUBJECT TERMS
attojoule, optoelectronics, nanophotonics, 2D material heterostructures, nanolasers

16. SECURITY CLASSIFICATION OF:			17. LIMITATION OF ABSTRACT	18. NUMBER OF PAGES	19a. NAME OF RESPONSIBLE PERSON
a. REPORT	b. ABSTRACT	c. THIS PAGE			POMRENKE, GERNOT
Unclassified	Unclassified	Unclassified	UU		19b. TELEPHONE NUMBER *(Include area code)* 703-696-8426

Standard Form 298 (Rev. 8/98)
Prescribed by ANSI Std. Z39.18

AFOSR Project Final Report

Report Date: February 28, 2019 (For the period of Dec.1, 2015 to Nov. 30, 2018)
Title: Single Sheet Lasers for Attojoule Optoelectronics
Grant Number: FA9550-16-1-0010
PM: Dr. Gernot Pomrenke, AFOSR/RTA1, gernot.pomrenke@us.af.mil
PI: Weidong Zhou, University of Texas at Arlington (UTA)
Department of Electrical Engineering, wzhou@uta.edu
Co-PI: Xiuling Li, University of Illinois Urbana Champaign (UIUC)
Department of Electrical and Computer Engineering, xiuling@illinois.edu
Co-PI: Shanhui Fan, Stanford University
Department of Electrical Engineering, shanhui@stanford.edu

Abstract and Major Contributions

The objective of this project is investigate laser scaling towards extreme energy efficiency. Over the last three years, we have investigated a range of photonic crystal cavities, including low index heterostructure photonic crystal cavities for the lateral confinement, Eigenvalue dynamics and gain/loss modulation in photonic crystal cavities for parity-symmetry systems, non-Hermitian perturbations on Weyl Hamiltonians with arbitrary topological charges. These cavities can all be integrated with suitable gain medium for novel laser devices with unique properties and potentially lower lasing threshold high energy efficiency.

Large area monolayer 2D material preparation and synthesis have also been investigated. Large area MoS2 MOCVD growth on patterned GaN substrates process was explored which shows great potential for direct growth of 2D material on photonic crystal cavities. Gold-mediated exfoliation and viscoelastic stamp transfer technique was developed for large area (over 100 mm sized) monolayer 2D material preparation and integration processes. In collaboration with NSF 2DCC-MIP national user facility at PSU, wafer scale monolayer 2D materials were also used in the project for the demonstration of large array size lasers based WS2 material. 2D material transfer-printing process on an automatic assembly platform was also developed for high quality 2D material transfer printing and stacking.

High quality SiN material and cavities were also developed for the demonstration of laser devices. Optically pumped room temperature lasers were achieved with low lasing threshold and high directional beam, based both on exfoliated and large area CVD WS2 materials on heterostructure photonic crystal cavities. Detailed investigations were carried out on the laser cavities and lasing characteristics, including spectral outputs, polarization, optical beam divergence angle, and lifetime measurements.

Specific Research Tasks and Summary by Year:

During Year One, we have carried out the proposed research tasks and made the following progresses: (1) Design a unique defect-free photonic crystal cavities for single-sheet active material lasers (Fan); (2) Eigenvalue dynamics and gain/loss modulation in photonic crystal cavities for parity-symmetry systems (Fan); (3) Developed silicon nitride fabrication processes (Zhou); (4) Designed and demonstrated high quality factor silicon nitride cavities operating at visible wavelength (Zhou-Fan); (5) Large area MoS2 MOCVD growth on patterned GaN substrates (Li-Zhou); (6) Developed 2D material preparation and integration processes based on gold-mediated exfoliation and viscoelastic stamp transfer technique (Zhou-Li-Fan); (7) Demonstrated emission enhancement of 2D material integrated on photonic crystal cavities (Zhou-Li-Fan).

During Year Two, we have made the following progresses: (1) Achieving arbitrary control over pairs of polarization states (modeling) using complex birefringent metamaterials (Fan); (2) Size scaling and radiation pattern control in heterostructure PhC cavities (Zhou-Fan); (3) 2D material synthesis on patterned GaN substrates (Li); (4) Optically pumped room temperature low threshold lasing action from 2D-Heterostructure PhC cavities (Zhou-Fan-Li); and (5) Gain/loss modulation demonstration experimentally on WSe_2 coupled cavities (preliminary).

During Year Three, we have made the following progresses: (1) Effects of non-Hermitian perturbations on Weyl Hamiltonians with arbitrary topological charges (Fan); (2) Pulse shortening in an actively mode-locked laser with parity-time symmetry (Fan); (3) Confirmation and direct measurement of the far field radiation pattern of the room temperature optical pumped monolayer WS2 PCSEL (Zhou); (4) Engineering the far field radiation pattern of the heterostructure PhC cavities (Zhou-Fan); (5) Room temperature lasing in the defect state of synthesized monolayer WS2 (Zhou, collaborated with Penn State); (6) Development of 2D material transfer-printing process on an automatic assembly platform.

Contents

1. Photonic crystal heterostructure for a single-sheet active material laser (Fan Group, Year One)

Two-dimensional transition metal dichalcogenide (TMDC) materials have opened a promising perspective in the domain of on-chip photonic technologies due to their small size, strong optical absorption, and possibility for integration on silicon-based substrates. With this motivation, we have theoretically studied and optimized a Photonic Crystal (PhC) structure in a silicon nitride (Si_3N_4) slab that can lead to low-threshold lasing when covered by a MoS_2 layer. The theoretical study took into account all practical considerations, most importantly: TE-like mode for stronger interaction with the 2D material; in-plane concentration of the electric field within a region of linear size of the order of 10μm; and a high quality factor (Q). The starting point was the study of the photonic band diagrams of various PhCs formed by a lattice of air-holes in a Si_3N_4 slab on quartz. Rectangular, honeycomb, and hexagonal lattices were studied, and all were found to support dark modes (Q going to infinity) at the Γ-point. However, the hexagonal lattice was found to be superior in that said dark mode is non-degenerate and well-separated from the rest. The band structure in question is shown in Figure 1(a), and the displacement field of the lowest-frequency mode at k = Γ is shown in panel (b). This mode was found to be dark, and was therefore used as a starting point for a high-Q, localized, heterostructure mode. The PhC heterostructure was formed by a central region of hole radius $r = 0.24a$, a transition region of radius $r = 0.22a$, and an outer region with $r = 0.20a$. The size of the regions was optimized for maximum finite-difference time-domain (FDTD)-computed Q, and a high value of 22,600 was found for 10 periods of holes in the core region and 6 periods in the transition region. The displacement field profile of this particular design is plotted in Figure 1(c), and this simulated mode fits all the experimental requirements. The structure will therefore be tested experimentally, and we expect to achieve a small-footprint, low-threshold, on-chip laser.

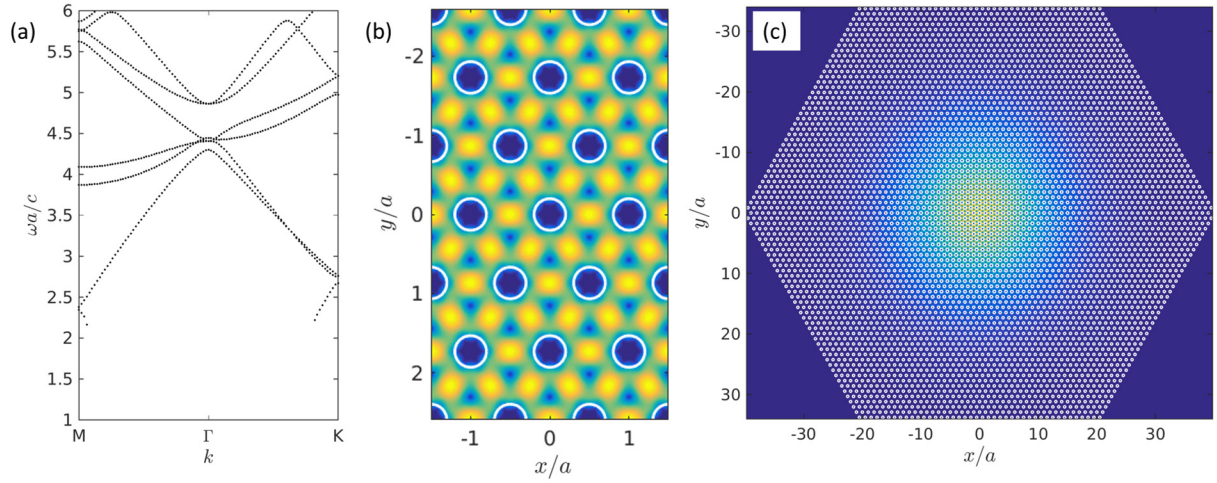

Figure 1: (a) Photonic band structure for the quasi-TE modes of a hexagonal lattice of air holes of radius $r = 0.24a$ in a Si_3N_4 slab on quartz (a is the lattice constant). (b) Displacement field profile of the lowest-frequency mode at k = Γ. (c) Localized field profile of a heterostructure mode based on the lowest-frequency dark mode at Γ (see text).

2. Summary of Eigenvalue dynamics and non-uniform distributions of gain and loss in PhCs (Fan Group, Year One)

Over the past few decades, significant progress has been made in understanding the optical properties of dielectric media containing different patterns of high and low index regions, such as the band structure of photonic crystals and the eigenvalue distribution of random media. However, one of the important properties of optical media is the relative ease with which one can add gain and loss. Recently, explorations into systems which are invariant under parity and time reversal symmetries, which contain patterned gain and loss, have revealed exotic phenomena and systems, such as lasers which turn off as additional gain is added to the system, and band-merging in photonic crystals with patterned gain and loss. In our two recent works [1, 2], we have sought to understand which of these exotic properties are unique to systems which strictly obey parity-time symmetry, and which properties are generally present in non-Hermitian systems with spatially patterned gain and loss.

In "Eigenvalue dynamics in the presence of non-uniform gain and loss," we derived the general conditions under which counterintuitive behaviors, such as the aforementioned reverse-pump dependence in lasers, can be observed. In doing so, we demonstrated that such phenomena are not limited to systems which are parity-time symmetric. For example, consider the system consisting of three coupled cavities shown in Figure 2(a). At first, gain is only added to the center cavity, and the system reaches the lasing threshold. However, as the gain is added to the left and right cavities while the gain in the center cavity is held constant, the laser turns off, until the gain in the three cavities becomes nearly uniform, at which point the laser turns back on again. This example illustrates the general principle that any laser system comprised of constituent sections with independently tunable gain can be configured to display reverse-pump dependence.

In "Effects of non-uniform distributions of gain and loss in photonic crystals," we derived a perturbation theory for understanding the effects of patterned gain and loss in photonic crystals upon the band structure of the crystal. This perturbation theory identifies regions in wavevector space where the addition of gain and loss to the photonic crystal either results in strong coupling between the bands, or creates new gaps in the band structure. Such strongly coupled regions can be observed in Figure 2(c), (d) along the $k_x = \pi/2a$, where a is the lattice spacing. Finally, we identify a conserved quantity that the frequencies of the non-Hermitian system must obey.

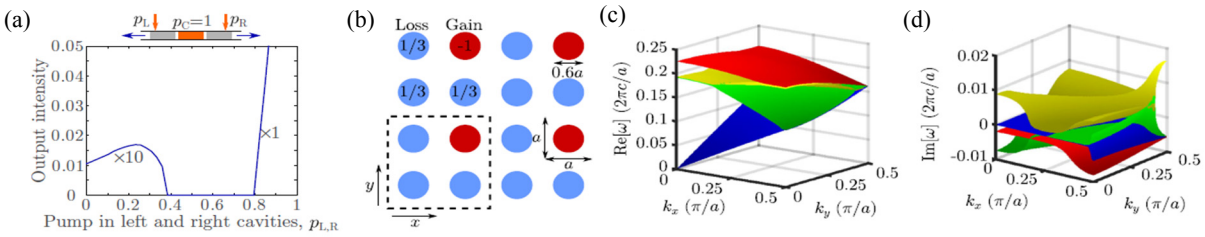

Figure 2: (a) Full-wave simulations of the outgoing intensity from the three-cavity system depicted schematically as the gain in the center cavity is held constant, while the gain in the left and right cavities is increased. (b) Schematic of a 2D photonic crystal formed of dielectric circular rods embedded in air. Some of these rods contain gain (red), while the remainder contains loss (blue), such that the sum of the gain and loss within a single primitive cell of the system (black dashed box) is zero. (c), (d) The real and imaginary components of the first four transverse magnetic bands of this photonic crystal.

3. Achieving Arbitrary Control over Pairs of Polarization States Using Complex Birefringent Metamaterials (Fan Group, Year Two)

Polarization is one of the fundamental properties of light, and control over the polarization is paramount in many optical communications and imaging applications. Conventionally, the polarization of a signal is manipulated through the use of birefringent materials. For lossless birefringent media, with proper choice of material parameters and propagation distance, it is always possible to convert an input polarization to an arbitrary output polarization. However, once the response to such an input polarization is determined, the output polarization is no longer arbitrary for any other input polarization. That is because for lossless medium always transfer a pair of orthogonal polarizations to another pair of orthogonal polarizations.

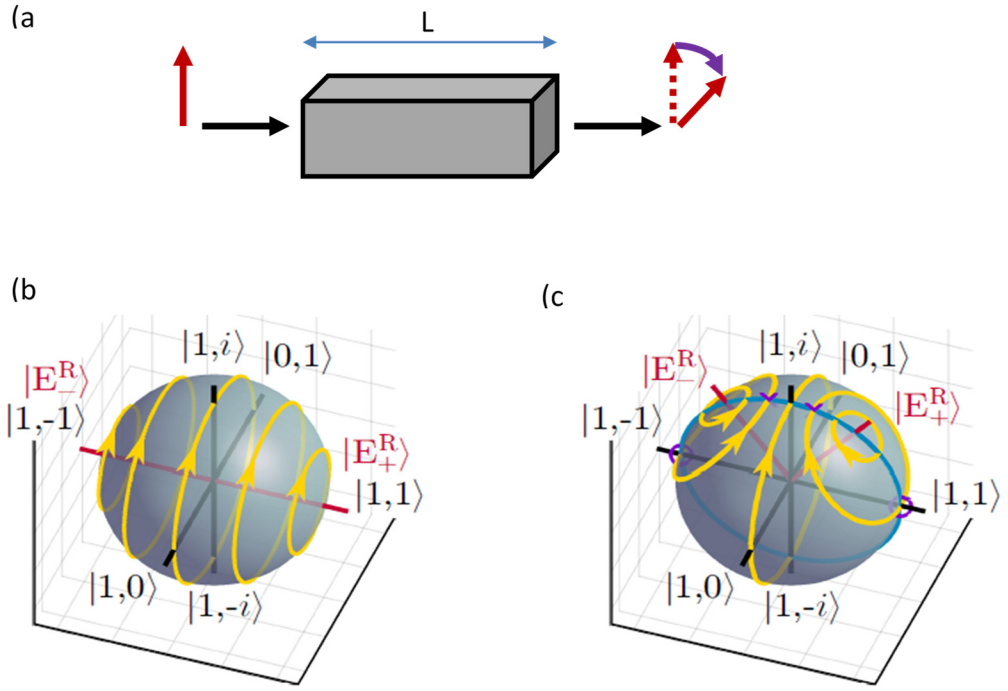

Figure 3: (a) Polarization rotation as light passes through a bi-refrigent media. (b) Conventional bi-refrigent medium preserves modal orthogonality. Shown here are the trajectory of the output polarization as the length of media L varies. In a conventional medium, the trajectory forms concentric circles. (c) Our complex symmetry meta-material breaks the orthgonality constraint, and enables arbitrary control of a pair of polarizations.

In a paper published in Physical Review Letters [3], we develop a class of novel meta-material that overcomes the limitation of conventional birefringent media. This class of meta-material exhibits loss for one of the polarization, and a compensating gain for a polarization that is orthogonal to it. We show that such a meta-material enables arbitrary control over pairs of polarization states. For a pair of arbitrary input polarizations, one can generate an arbitrary pair of output polarization. Achieving such polarization control has significant implications for a wide range of technologies. For example, with this capability, one can map two polarizations that are close to each other into two orthogonal polarizations, which may facilitate the detection of small polarization changes, such as those arising from the imaging of biological tissues and thin films. Likewise, the ability to completely separate nonorthogonal polarization states could enable new multiplexing schemes in optical communications networks beyond what is currently possible.

4. Effects of non-Hermitian perturbations on Weyl Hamiltonians with arbitrary topological charges (Fan Group, Year Three)

The study of topological systems represents an important frontier in both condensed-matter physics and photonics, as these systems can possess exotic electronic and photonic states. A defining feature of these unusual topological states is their protection against many forms of disorder. One important class of three-dimensional topological systems are Weyl semimetals, which possess a set of isolated degeneracies in their band structure. It is known that in a system with Weyl points, any Hermitian perturbation can only change the location of the Weyl points and cannot remove or create them. Such Hermitian perturbations are common in electronic systems. On the other hand, in photonic systems there are many perturbations, such as material gain and absorption, as well as radiative outcoupling, which break hermiticity. Moreover, many recent studies have indicated that introducing non-Hermitian perturbations in topologically trivial systems can result in unusual phenomena, such as promoting single mode operation in lasers, loss-induced transmission in waveguide arrays, reverse pump dependence in lasers, and control over pairs of polarization states. Therefore, it is important to understand how non-Hermitian perturbations influence the properties of topologically nontrivial systems.

In our recent paper (Cerjan et al., Phys. Rev. B **97** 075128 (2018)), we provide a systematic study of non-Hermitian topologically charged systems and uncover a set of remarkable effects in this class of systems. First, we analytically prove that in the presence of arbitrary non-Hermitian perturbation, a Weyl point with an arbitrary charge transforms into a closed one-dimensional exceptional contour, with the topological charge preserved on the contour. However, such a contour need not form a single ring, but it can take a more complex shape when the charge is greater than 1. Second, we demonstrate that, in contrast to Hermitian systems, the addition of gain and loss allows for an alternative mechanism by which the topological charge in the system can dissipate: when two oppositely charged exceptional contours touch, the resulting exceptional contour does not possess a Berry charge. Unlike a Hermitian system, here the disappearance of the charge is not associated with the opening of the band gap. Third, in such systems the upper and lower bands associated with the exceptional ring are two branches of the same Riemann sheet, and so it is possible to follow a smooth path through the exceptional contour and transition from being on the upper band to being on the lower band. Finally, all of these effects can be demonstrated in realistic photonic and acoustic systems. Thus, our results highlight significant opportunities for exploring topological physics in non-Hermitian systems.

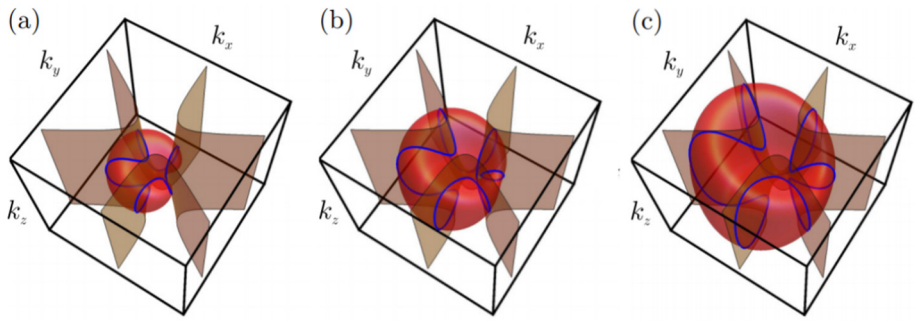

Figure 4: (a) Exceptional contour associated with a charge-2 Weyl point with wave-vector-dependent gain and loss added, with increasing strength in (a)-(c). The exceptional contour (blue) is defined by the intersection of the two plotted surfaces (red and orange). As can be seen, a portion of the exceptional contour splits off in (b), yielding two independent exceptional contours. When this happens, the smaller exceptional contour does not carry a Berry charge, while the larger exceptional contour still carries a Berry charge of 2.

5. Pulse shortening in an actively mode-locked laser with parity-time symmetry (Fan Group, Year Three)

Based on the realization that a non-Hermitian Hamiltonian with parity-time (PT) symmetry can have a purely real eigenvalue spectrum, there is now a large body of studies exploring physical phenomena related to PT symmetry in a variety of physical systems. As one significant recent development, lasing action in PT-symmetric systems has been explored, where enhanced control of continuous-wave lasing is achieved due to spontaneous breaking of the PT symmetry.

In our recent article (Yuan et al., APL Photonics **3** 086103 (2018)), as a step further to exploit the concept of PT-symmetry in lasing systems, we consider an actively mode-locked laser system exhibiting PT symmetry. Active mode locking is an important technique for generating short pulses from a laser. A standard actively mode locked system consists of a ring resonator incorporating an amplitude modulator. Short pulses can be generated when the modulation frequency matches the free spectral range of the ring. Although the shortest pulses in mode-locked systems are generated with passive mode locking techniques, in many situations, active mode locking is still extensively applied. For example, it has been noted that active mode locking is the method of choice for generating short pulses in quantum cascade lasers due to the unique gain characteristics of quantum cascade lasers.

In our work, we consider a system consisting of two rings coupled together. Within each ring, there is an amplitude modulator. Such a system can be described by a Hamiltonian that has a PT symmetry when the phases of the modulators differ by π. We show that, with the same modulation frequency and gain bandwidth, a much shorter pulse can be generated in the two-ring system as compared to the one-ring system, due to a spontaneous breaking of the PT symmetry. This expands the potential application of the concept of PT symmetry in the lasing system by showing that these concepts can be fruitfully applied in the pulsed laser system.

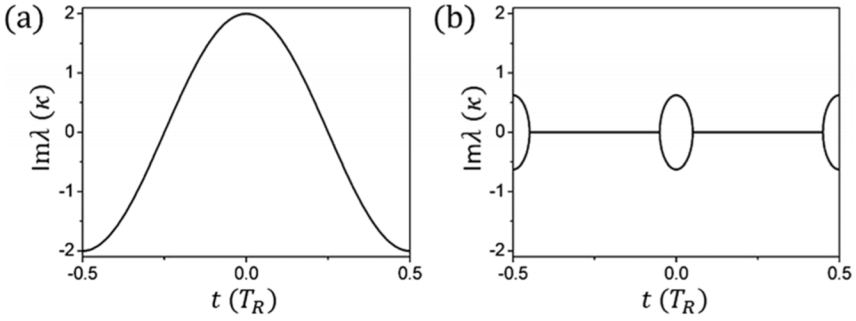

Figure 5: (a) Imaginary part of the synthetic-space band structure in a single ring resonator undergoing amplitude modulation. (b) Imaginary part of the band structure in two ring resonators with the PT symmetry. The narrowing of the time-window with gain due to the PT symmetry leads to the active pulse shortening.

6. Development of silicon nitride based fabrication processes (Zhou Group, Year One)

To fabricate 2D material based lasers working at the visible wavelength, a complete set of silicon nitride based processes was developed in-house at UTA. Silicon nitride film is deposited using the Tystar Tytan low pressure chemical vapor deposition (LPCVD) furnace system, in which dichlorosilane (SiH_2Cl_2) and ammonia (NH_3) are used as sources for the silicon and

nitrogen to achieve optimum LPCVD conditions for improved thickness uniformity and substrate spacing sensitivity. We are able to deposit silicon nitride films with the thickness of over 300 nm on silicon and quartz substrates without generating cracks in the following processes. The measured refractive index and extinction coefficient of the silicon nitride film are plotted in Figure 6(a).

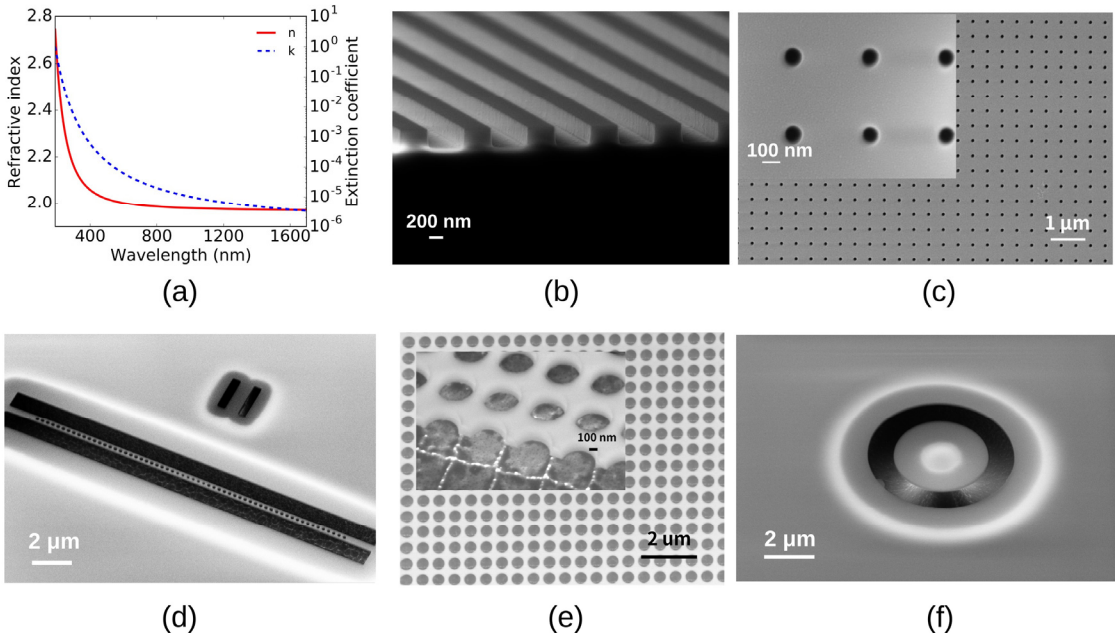

Figure 6: Demonstration of silicon nitride based fabrication process developed at UTA. (a) Measured refractive index and extinction coefficient of the LPCVD silicon nitride film. (b)-(f): SEM images of silicon nitride gratings, 2D photonic crystal filters, nanobeam cavities, suspended membrane reflectors and microdisk cavities.

Device patterning is performed by electron beam lithography (EBL) on a Zeiss 1540 XB Cross Beam SEM with Nanometer Pattern Generation System (NPGS). ZEP520A e-beam resist is used for its high resolution and good etching resistance. The patterned sample is developed in cooled N-Amyl acetate for improved contrast and sidewall smoothness. As shown in Figure 6 (c), sub-100 nm diameter holes can be patterned and etched.

The silicon nitride etching process was developed on a Trion inductively coupled plasma reactive ion etcher (ICP-RIE). A gas combination of sulfur hexafluoride (SF_6), fluoroform (CHF_3) and helium were used and fine-tuned to achieve a vertical sidewall and a reasonable selectivity versus ZEP520A (1:1.2). In order to create silicon nitride membranes suspended over silicon substrates, an isotropic SF_6 based silicon etching process was also developed. The selectivity of silicon versus silicon nitride and ZEP520A was measured to be 150:1 and 100:1 respectively. Thus, the silicon substrate can be undercut without damaging the patterned silicon nitride film.

Based on the processes developed, we are able to fabricate high quality silicon nitride based nanophotonic devices at UTA, as shown in Figure 6, where gratings (b), 2D photonic crystal filters (c), suspended 1D photonic crystal nanobeam cavities (d), 2D photonic crystal membrane reflectors (e) and microdisk cavities (f) are demonstrated.

7. Demonstration of silicon nitride cavities at visible wavelengths (Zhou-Fan Groups, Year One)

Having established the fabrication processes of silicon nitride, we designed and demonstrated a series of photonic crystal based cavities, including defect free 2D photonic crystal filters, which is targeting large area, synthesized 2D material, laterally confined heterostructure cavities, which is suitable for the high quality, limited size exfoliated 2D material, and photonic crystal nanobeam cavities, which has a small mode volume and is promising for low threshold lasing.

a. Defect free large area 2D photonic crystal filters

Based on the proposed structure, first we designed a cavity with a large area defect free 2D photonic crystal filter. A square lattice photonic crystal of the period a = 440 nm was considered. Figure 7(a) shows a side-view sketch of the photonic crystal filter, where 160 nm of silicon nitride film is deposited on a double side polished quartz wafer. Single crystal quartz, despite of its slightly higher refractive index (n = 1.53), is preferred over fused silica (n = 1.46) due to its better thermal properties for the LPCVD process.

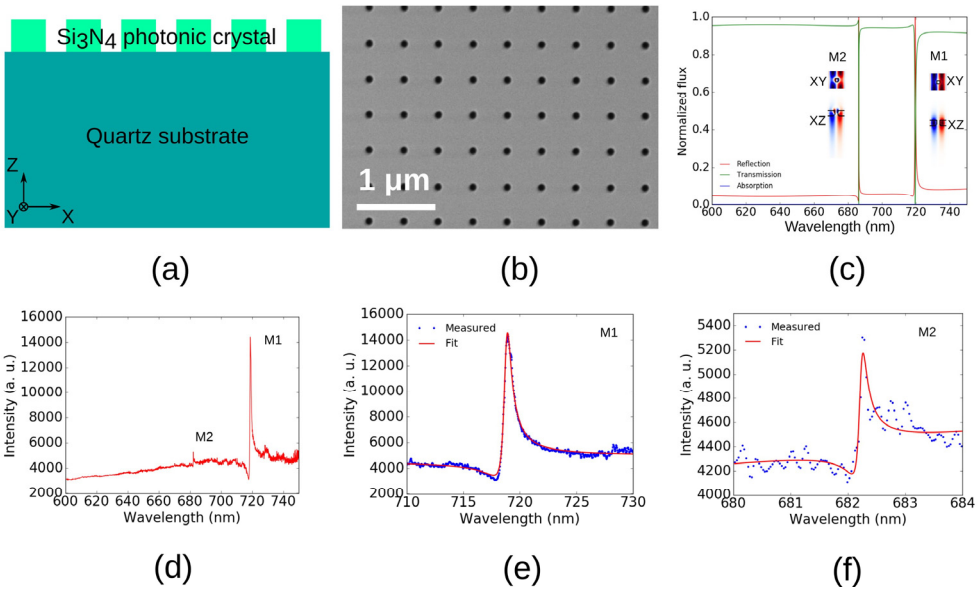

Figure 7: Defect free 2D photonic crystal cavities: (a) Schematic of patterned silicon nitride on quartz substrate. (b) Top view SEM image of the fabricated defect free 2D photonic crystal. (c) RCWA simulation of the transmission and reflection spectra at normal incidence. The insets show FDTD simulated magnetic field distribution *Hz* of the resonant modes. (d) Measured reflection spectrum of the fabricated photonic crystal. (e), (f) Fitting of the resonant peaks M1 and M2 in (d).

S^4, a freely available rigorous coupled-wave analysis (RCWA) package developed by co-PI Fan's group [4], was used to calculate the transmission and reflection spectra of the 2D photonic crystal filter at normal incidence. The measured material parameters in Figure 7(a) were used in the simulation. The results are shown in Figure 7(c). Two Fano resonance peaks are visible in the spectra, corresponding to two guided resonance modes, marked as M1 and M2, of the photonic crystal at Γ point. Finite-difference time domain (FDTD) method [5] was used to calculate the mode patterns, resonant wavelengths and quality factors, shown in the inset of Figure 7(c) and Table 1 respectively. The resonant modes have the field distribution concentrated to the silicon

nitride slab. The mode M2 is within the emission spectrum of monolayer MoS_2 and has a high quality factor of over 6000.

Table 1: Comparison of simulated and measured results of the photonic crystal filters.

	Period	Radius	Mode	Wavelength	*Q* factor
Simulation	440 nm	50 nm	M1	720.05 nm	1112
			M2	686.96 nm	6405
Experiment	441 nm	30 nm[a]	M1	719.91 nm	919
			M2	682.25 nm	4259

[a] Parameter used in the pattern file.

Figure 7(b) shows the top view of the fabricated sample. The geometric parameters for fabrication are listed in Table 1. Note that the hole radius used for patterning is smaller than the designed value due to the size broadening in the following developing and etching processes. The full size of the fabricated photonic crystal lattice is 230 μm × 230 μm. The fabricated sample was characterized by white light reflection measurement on a home-built microscope. A drop of index-matching gel that has a refractive index of 1.52, which matches that of the quartz substrate was applied to the polished backside of the sample, which reduces the FP oscillations from the finite substrate thickness. White light from a halogen lamp (Ocean Optics DH-2000) was polarized and used to illuminate a 100 μm diameter pinhole, which was focused by a 4×, 0.1 numerical aperture (NA) objective lens to a 180 μm spot on sample that was within the photonic crystal area. The reflected signal was collected by the same objective lens and redirected to a monochromator (Horiba iHR-550). The measured normal incidence reflection is shown in Figure 7(d).

In the measured spectrum two resonance features that are close to the simulated wavelengths can be observed, which are also marked as M1 and M2, respectively. By fitting the two measured peaks with Fano lineshape, as shown in Figure 7(e) and (f), and comparing the fitted wavelengths and quality factors listed in Tab. 1, it can be seen that the resonant wavelengths and quality factors agree well between the simulation and experiment. Thus, we have realized a defect free large area 2D photonic crystal filter that can be used as a laser cavity for transferred or directly grown large area 2D material films.

b. Laterally confined heterostructure 2D photonic crystal cavities

As the CVD grown 2D materials generally have inferior photoluminescence performance compared to exfoliated 2D material flakes, and the exfoliated 2D material flakes have a low yield and small lateral size (ranging from a few micrometers to tens of micrometers). We considered implementing lateral confinement to the guided resonance based 2D photonic crystal, which confine the resonant mode within a small region while maintaining a high quality factor. Compared to the defect cavities in band gap type 2D photonic crystal, this cavity has the advantage of close to vertical direction emission and has better out coupling efficiency.

Consider a hexagonal lattice of air holes on a 160 nm thick silicon nitride slab on quartz substrate, the first order TE mode at Γ point is a “dark mode” [6-8] which do not couple to the radiation continuum due to symmetry mismatch. As the wave vector approaches Γ the vertical quality factor of the dark mode approaches infinity. This dark mode was used for vertical

confinement and the lateral confinement was provided by a mode gap from a gentle modulation of the hole radii. In our designs the hexagonal lattice was chosen over the square lattice due to less lateral leakage at the corners, resulting in a higher quality factor.

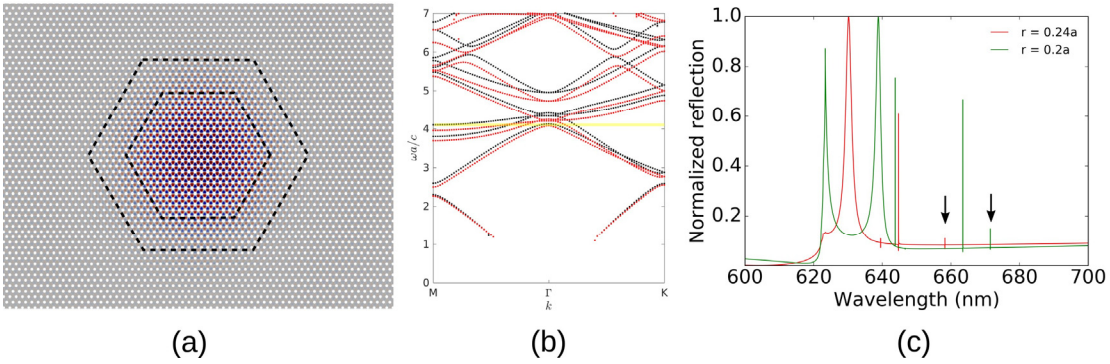

Figure 8: Design of the lateral confined heterostructure photonic crystal cavities: (a) FDTD simulated magnetic field *Hz* of the resonant mode, overlaid with the heterostructure photonic crystal. Regions of different hole radii are separated with dashed lines. (b) Band structure of the cavity core (black) and cladding (red) regions. (c) Simulated reflection spectra of the core (red curve) and cladding (green curve) photonic crystals. The arrows indicate the positions of the first order dark mode.

The cavity structure is shown in Figure 8(a). The photonic crystal lattice is divided by the hexagonal dashed lines into three regions: the cavity "core region" in the center, the "cladding region" at the outside and the "transition region" in between. The period of the holes is kept constant at a = 470 nm while the hole radii r is slightly different for each region. To be specific $r_{core} = 0.24a$, $r_{trans} = 0.22a$, and $r_{clad} = 0.2a$.

Figure 8(b) shows calculated band diagram for both core (black) and cladding (red) photonic crystals. As the first order dark mode is non-degenerate, a mode gap (yellow) can be seen near Γ where the modes of the core region cannot propagate in the cladding region thus are laterally confined. Figure 8(c) shows calculated near-normal incidence (tilted by 0.1° to excite the dark modes) reflection spectra of both core (red) and cladding (green) photonic crystals. The positions of the first dark mode considered are marked by black arrows.

The cavity resonant modes are simulated by 3D FDTD. Figure 8(a) shows the *Hz* distribution of the fundamental mode, which is well confined within the core region. To clearly visualize the field the outside of the cladding has been cropped. In our simulations a cladding of 20 to 30 periods is sufficient for confinement. Figure 9 shows the influence of lateral confinement. The cavity shown in (a) is a heterostructure cavity while the cavity in (b) is defect free except for the finite size, and all the holes have $r = 0.24\ a$, the same as the core region of (a). Other than that the two cavities are identical. From the calculated field amplitude we can see that while both cavities have the field confined vertically in the silicon nitride slab, the mode of the cavity with heterostructure has a negligible lateral leakage compared to the one without. The calculated quality factor is about 30,000 for the heterostructure cavity and about 600 for the defect free one.

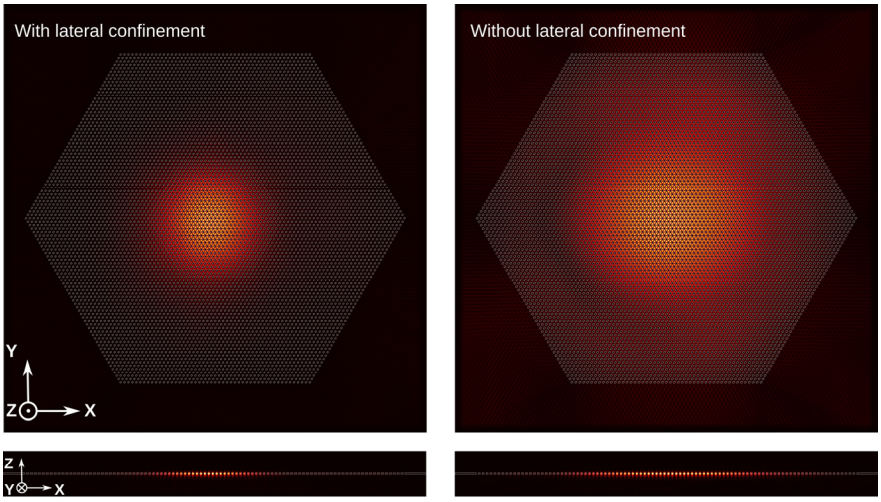

Figure 9: FDTD calculated Hz field amplitude of heterostructure (a) and defect free (b) cavities

A series of heterostructure cavities targeting either MoS_2 or WSe_2 emission wavelengths have been fabricated. Figure 10(a) shows an SEM image of a typical cavity of the full size close to 30 μm, which makes it possible to use exfoliated 2D material flakes. The fabricated cavities were measured with cross-polarized white light reflection method, where two polarizers with the polarization directions crossed to each other were inserted in the light path. One is placed at the source and the other is placed near the detector. Only the reflected signal from the cavity, which changes the polarization state of the incident light due to fabrication error and non-perfect perpendicular incidence, is able to pass the second polarizer and be detected by the monochromator. The incident light was focused to an 18 μm diameter spot by a 10×, 0.25 NA lens. And a variable iris is placed near the back aperture of the objective lens to further reduce the NA of the lens, eliminating large angle scattered signal coming from the bulk photonic crystal modes away from Γ point. This configuration enhanced the signal-to-noise ratio for detecting the resonant peaks.

Representative spectra for both MoS_2 and WSe_2 targeted cavities are shown in Figure 10(b) and (c). Apart from the broad peaks at shorter wavelengths, which comes from the low *Q*, bright modes of the photonic crystals. A series of sharp peaks are also visible. These are the cavity modes of interest that originate from the first order dark mode of the photonic crystal in the cavity core region. The cavity do support higher order modes due to the large core sizes (vary from 10 to 30 periods in our simulation and experiment). Since the band of interest has a maximum at the Γ point band edge. The high order modes, which are farther away from Γ compared to the fundamental mode, have longer resonant wavelengths. And as the high order modes are away from Γ, the modes become less and less "dark", i.e. more leaky in the vertical direction, thus have a lower quality factor. And it can also be observed that the high order mode peaks are split, which comes from the broken symmetrical degeneracy due to fabrication disorder.

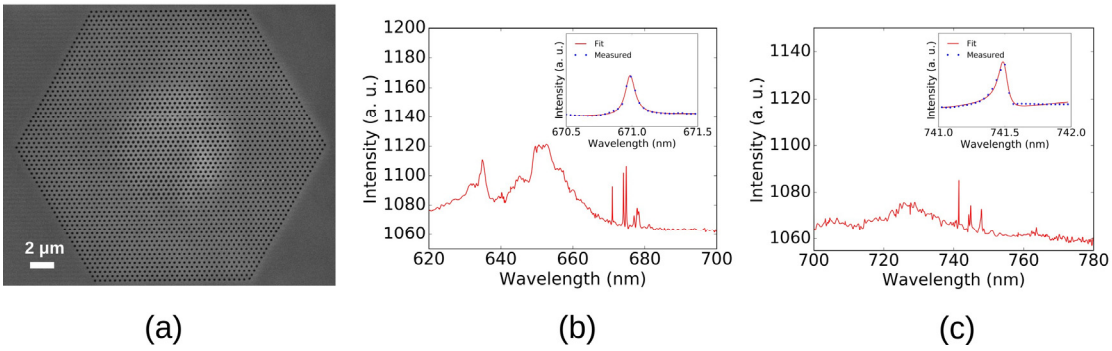

Figure 10: Experimental demonstration of the lateral confined heterostructure photonic crystal cavities: (a) SEM image of a fabricated heterostructure cavity sample. (b), (c) Measured cross polarized reflection of heterostructure cavities resonating at MoS_2 and WSe_2 emission wavelengths respectively. The insets show fitting of the fundamental cavity modes.

The peaks of the fundamental modes are fitted and plotted in the insets of Figure 10(b) and (c). The fitted wavelengths and quality factors are $\lambda_1 = 670.98$ nm, $Q_1 = 7461$ and $\lambda_2 = 741.50$ nm, $Q_2 = 8760$. It should be noted that the measured linewidth is limited by the resolution of our monochromator.

In conclusion, by incorporating lateral confinement, we have designed and demonstrated vertical emitting photonic crystal cavities that have a high Q and reasonable size which enables the use of high quality exfoliated 2D material flakes.

c. Photonic crystal nanobeam cavities

We also investigated 1D photonic crystal nanobeam cavity for its high quality factor and small mode volume, which is beneficial for the limited size of exfoliated 2D material flakes and low threshold lasing.

The photonic crystal nanobeam cavity design is based on a waveguide with 1D periodicity. Targeting the emission wavelength of monolayer MoS_2, a lattice constant $a = 280$ nm is chosen. The width and thickness of the silicon nitride waveguide are 378 nm and 160 nm respectively. A waveguide suspended in air is considered due to the low refractive index of silicon nitride. The calculated dispersion for different hole sizes are plotted in Figure 11(a). The red and green curves are the waveguide modes of the unit cells at the edge and center part of the cavity, which have different hole radii. The calculated mode near the band edge of the cavity center modes falls within the gap between the cavity edge modes, thus will be confined within the cavity center. A gradual modulation of hole radii from the cavity center to the edge is used to minimize the leakage [9].

As the second order waveguide mode (air band) is used in the design, the resulting cavity has the electric field concentrated in the air holes, which is beneficial for interacting with the integrated 2D material. The cavity resonance is simulated by 3D FDTD and plotted in Figure 11(b) with $\lambda = 665.56$ nm, $Q = 100{,}000$.

For fabricating the photonic crystal nanobeam cavities, 160 nm of silicon nitride was deposited on a bulk silicon wafer by LPCVD. After patterning and etching the silicon nitride layer. The isotropic silicon etching process introduced in Section 1 was used to undercut the silicon substrate with the presence of the e-beam resist ZEP520A. After releasing the nanobeam cavities,

ZEP520A was removed in hot N-Methylpyrrolidone and the sample was cleaned in oxygen plasma to remove residues. Figure 11(c) shows the top view SEM image of the suspended nanobeam cavity.

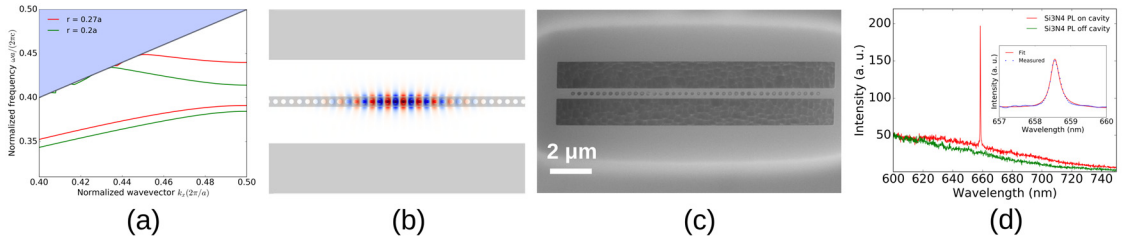

Figure 11: Design and demonstration of photonic crystal nanobeam cavities: (a) Simulated band diagram of the 1D photonic crystal. (b) Simulated field distribution *E*y of the nanobeam cavity resonant mode. (c) Top view SEM image of a suspended nanobeam cavity. (d) Measured silicon nitride fluorescence enhancement by the cavity.

The samples were characterized by utilizing the high Purcell factor (Q/V) of the cavity mode. Silicon nitride has a weak, broadband intrinsic fluorescence, which can be enhanced in the presence of a high Q/V cavity [9]. The sample was measured on a Thermo DXR Raman microscope with a 100×, 0.9 NA objective lens for focusing the excitation 532 nm laser and collecting the fluorescence signal. As shown in Figure 11(d), compared to the featureless off-cavity emission spectrum, a distinguished resonant peak can be observed in the on-cavity emission spectrum. The peak was fitted and plotted in the inset. The fitted quality factor is 2,152, which is limited by the 400 g/mm grating of the spectrometer.

In conclusion, high Q/V photonic crystal nanobeam cavities have been designed and demonstrated, which is a promising 2D material laser cavity candidate targeting low threshold lasing.

8. Radiation pattern control in heterotructure PhC cavities (Zhou-Fan groups, Year Two)

We investigated the size scaling properties and far field radiation pattern of the heterostructure PhC cavities. A sketch of the cavity is shown in Figure 12(a), where a silicon nitride layer on quartz is considered. Figure 12(b) shows a close-up view of the top right region of the cavity. The separation boundaries between the different regions of the cavity (denoted core, transition and cladding starting from the center) are indicated with the white dashed lines. The size parameters N_{core}, N_{trans} and N_{clad} are defined as the number of periods in each region starting from the center.

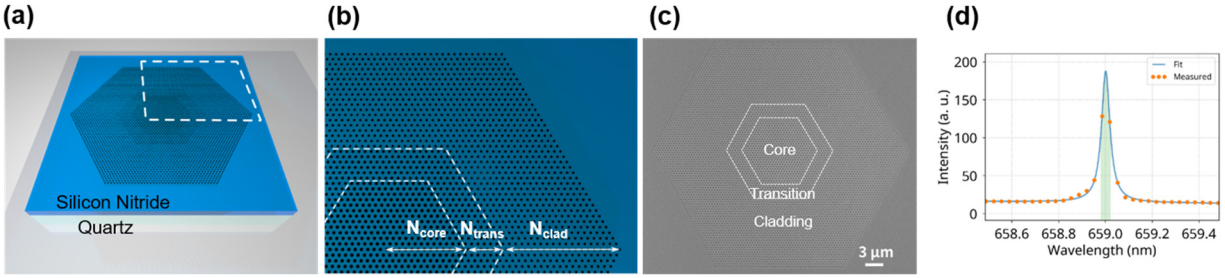

Figure 12: Design and experimental demonstration of a high *Q* heterostructure PhC cavity. (a) Sketch of the silicon nitride cavity on quartz. (b) Zoomed-in view of the different regions of the cavity and definitions of size parameters. (c) SEM image of a fabricated cavity. (d) Measured resonance and a Lorentzian fit showing a linewidth of 0.043 nm, corresponding to a *Q* factor of 15,000.

We fabricated a series of devices with the parameters listed in **Error! Reference source not found.**. Figure 12(c) shows a SEM image of a representative device. The fabricated cavities were characterized by measuring cavity-enhanced fluorescence of silicon nitride using a home-built micro-PL system. Figure 12(d) is the measured resonance spectrum of one device with fitted Q factor of 15,000, which is limited by our instrument measurement setup. A high Q factor is critical for achieving lasing in 2D materials due to the low confinement factor.

Table 2: Geometric parameters of the heterostructure cavity

t, thickness of the SiN layer	160 nm
a, period of the PhC	460 nm
R_{core}, radius of holes in the core region	115 nm
R_{trans}, radius of holes in the transition region	106 nm
R_{clad}, radius of holes in the cladding region	97 nm
N_{core}, size of the core region	3~21
N_{trans}, size of the transition region	2, 4, 6
N_{clad}, size of the cladding region	5~40

The FDTD simulated and experimentally measured size dependent cavity wavelengths and Q factors are shown in Figure 13(a)-(f). Figure 13(a) and (d) show the dependence on N_{core} in which N_{trans} and N_{clad} are fixed to be 6 and 40 respectively. We can see that the resonant wavelength decreases and the Q factor increases as the core size enlarges, which can be understood as the resonant mode approaching the Γ point at the top of the band. As the mode at Γ is a symmetry protected bound state in continuum (BIC state) the theoretical Q factor would diverge for an infinitely large lattice. The calculated N_{core} dependent Q factors in Figure 13(d) also show such a trend. However the experimentally measured Q is limited by our instrument which saturates at a larger N_{core}. In Figure 13(b) and (e) we fixed N_{core} = 12 and N_{trans} = 6 and scaled N_{clad}. As the cladding region increases, stronger lateral confinement effect results in a larger Q for both simulation and experiment. We also observed Q saturation for larger N_{clad} in both cases, which may be due to the fact that the vertical leakage becomes the limiting factor. In the cavity design point of view it means that, the vertical leakage, which equivalents to the output of a surface emitting laser would dominate the total leakage which would be beneficial for the efficiency of the laser. With a fixed N_{core}, the position of the mode in the band only has minimum change, which results the near-constant wavelengths for varying N_{clad} in Figure 13(b). In Figure 13(c) and (f), the effect of the size of the transition region is compared experimentally, in which N_{clad} is fixed to be 40 periods and different curves indicates N_{trans} to be 2, 4, and 6. While the effect of N_{core} follows the trend that was discussed above, a more gentle confinement by a larger transition region. [10] Unlike the heterostructure PhC cavities working near K point that relies the band gap effect for realizing lateral confinement [11], the presented heterostructure PhC cavity is based on the above line cone modes that near the Γ point, which would result in more desirable far field radiation properties (manuscript to be submitted). Figure 13(g) shows the FDTD simulated far field radiation pattern of a heterostructure PhC cavity in which most of the radiation concentrates to a small angle, which would form a better quality beam and lower the requirement of numerical aperture of the focusing lens for a small size of active region.

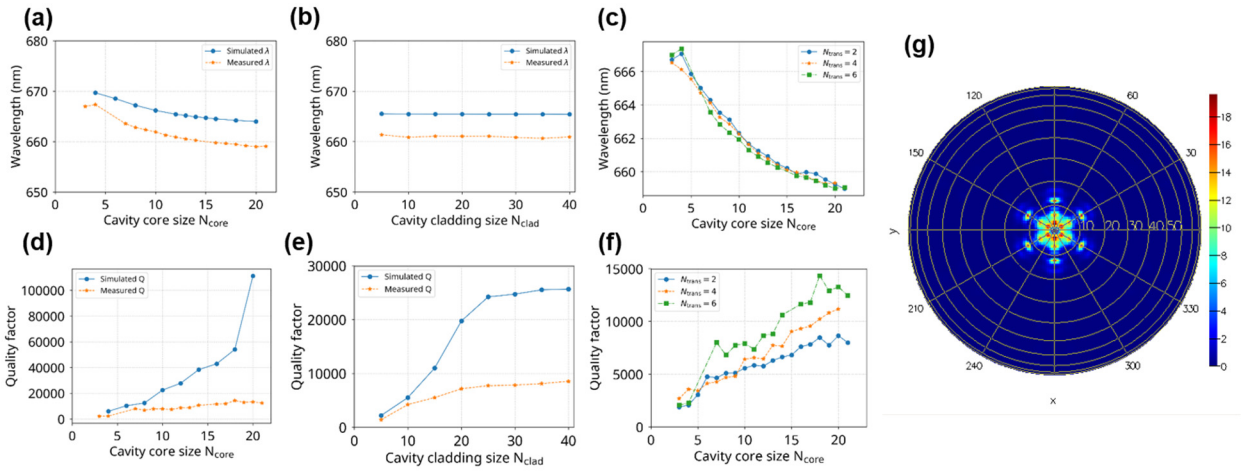

Figure 13: Size scaling and far field radiation pattern of the heterostructure PhC cavity. (a), (d) Core size dependent wavelengths and *Q* factors. (b), (e) Cladding size dependent wavelengths and *Q* factors. (c), (f) Core size dependent wavelengths and *Q* factors at various transition region sizes. (g) Simulated far field radiation pattern.

In conclusion, the *Q* factor of the heterostructure PhC cavity is optimized and the size scaling and far field radiation are also systematically investigated. The Γ point based heterostructure PhC cavity would have an efficient vertical emission and better beam quality than the PhC cavities working below the light line.

9. 2D material synthesis on patterned GaN substrates (Li-Zhou groups, Year One)

To integrate MoS_2 sheets directly on photonic crystal cavities, one aspect of the growth we are pursuing is van der Waals selective area epitaxy (vdW-SAE) by growing on patterned GaN patterned substrates. It is clear that epitaxy does matter for growth of 2D van der Waals sheets. Single crystal substrates are required in order to form domains of single crystals that are epitaxially aligned and capable of coalescing with minimum grain boundaries. To achieve high

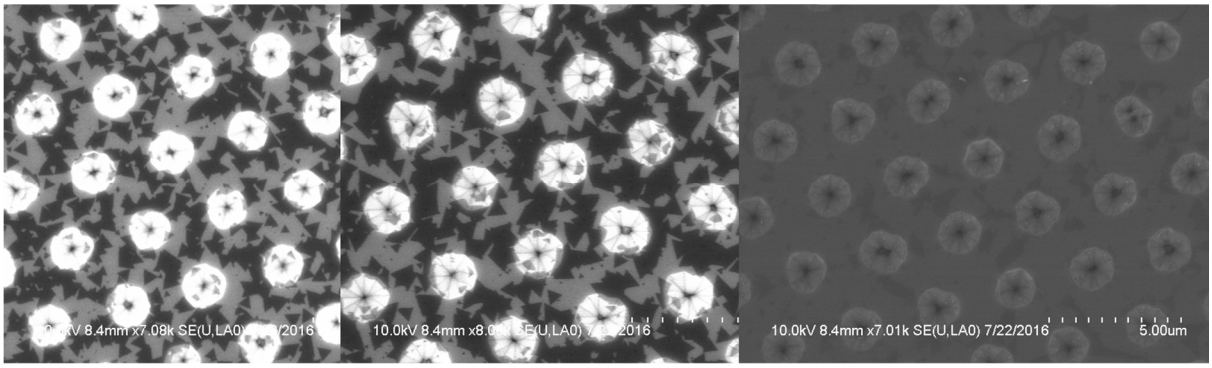

Figure 14: SEMs of MoS_2 growth evolution from individual triangles (left) to a continuous film covering the entire substrate (right).

quality epitaxial growth, one must explore independent and precise control of the injection, flow rate, pressure, temperature, pyrolysis, nucleation, diffusion, incubation, propagation of transition metal and group VI precursors and fragments.

We have successfully grown large areas of MoS_2 on un-patterned c-plane GaN and $In_xGa_{1-x}N$, and formed p-n junction diodes last year. For this period, the first patterned growth was performed on GaN grown on patterned sapphire substrates with arrays of sapphire pyramids of 1.8, 2.8, and 3 μm in height, width, and pitch, respectively. A two-step growth with a low temperature nucleation step was deemed critical to the formation of continuous MoS_2 film. Specifically, we inserted a 1 - 2 mins growth at 700 - 715ºC before ramping up temperature to 730ºC for further growth. Figure 14 shows the growth evolution of MoS_2 from individual triangles to a continuous film fully covering the substrate. We were able to achieve continuous coverage over ~1.5 x 1.5 cm^2 sample (limited by the reactor configuration) except the edges.

Based on spatial mapping of the characteristic Raman and PL peaks, it was found that MoS_2 on the patterned area shows stronger Raman intensity but weaker PL intensity, as shown in Figure 15. We believe this results from faster MoS_2 growth in the patterned area, leading to few layer

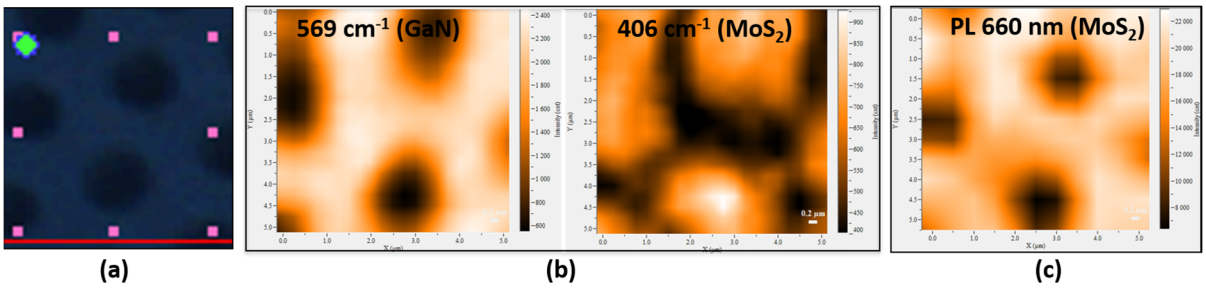

Figure 15: (a) Optical image of a continuous MoS_2 film grown on a patterned GaN/sapphire substrate where the dark area represents the pyramids, and the boxed area (5x5 μm^2) was mapped; (b) Raman maps at the GaN (569 cm^{-1}) and MoS_2 (406 cm^{-1}) peaks, respectively. (c) PL map of the same area at 660 nm (MoS_2).

formation, while only monolayer was formed in the planar GaN areas under this growth condition. The MoS_2 growth rate difference might be related to the surface orientation of the GaN substrate where the high index planes on the sidewalls of the patterned sapphire could promote faster growth. Ongoing and future work include growth study on substrates with other patterns including periodic perforated and porous GaN fabricated by etching. We hypothesize that the coalescence (through lateral growth) of single crystal domains could take place in free space (holey regions) with much less restriction on mismatch strain. Our ultimate goal is to enable (1) monolithic integration of 2D sheet with structures such as photonic crystal slab; and (2) mismatched van der Waals epitaxy by relaxing strain through free space (holey regions).

10. 2D material synthesis on patterned GaN substrates (Li-Zhou groups, Year Two)

The critical difference of our growth approach from most others in previous literature reports is epitaxy, pseudo-van der Waals (p-vdW) epitaxy of 2D sheets on 3D surfaces. Single crystal substrates (preferably lattice matched) are required in order to form domains of single crystals that are epitaxially aligned and capable of coalescing with minimum grain boundaries.

We have successfully demonstrated large area MoS_2 on c-plane GaN, including monolithically forming a p-n junction between n-MoS_2 and p-GaN, with an ideality factor of 1.3.

During the last performance period, we started pursuing pseudo-van der Waals selective area epitaxy (p-vdW SAE) by growing on patterned GaN (e.g. perforated structures), where the coalescence (through lateral growth) of single crystal domains could take place in free space

(holey regions). If successful, this approach will enable (1) monolithic integration of 2D sheet with structures such as photonic crystal slab; (2) mismatched van der Waals epitaxy by relaxing strain through free space (holey regions).

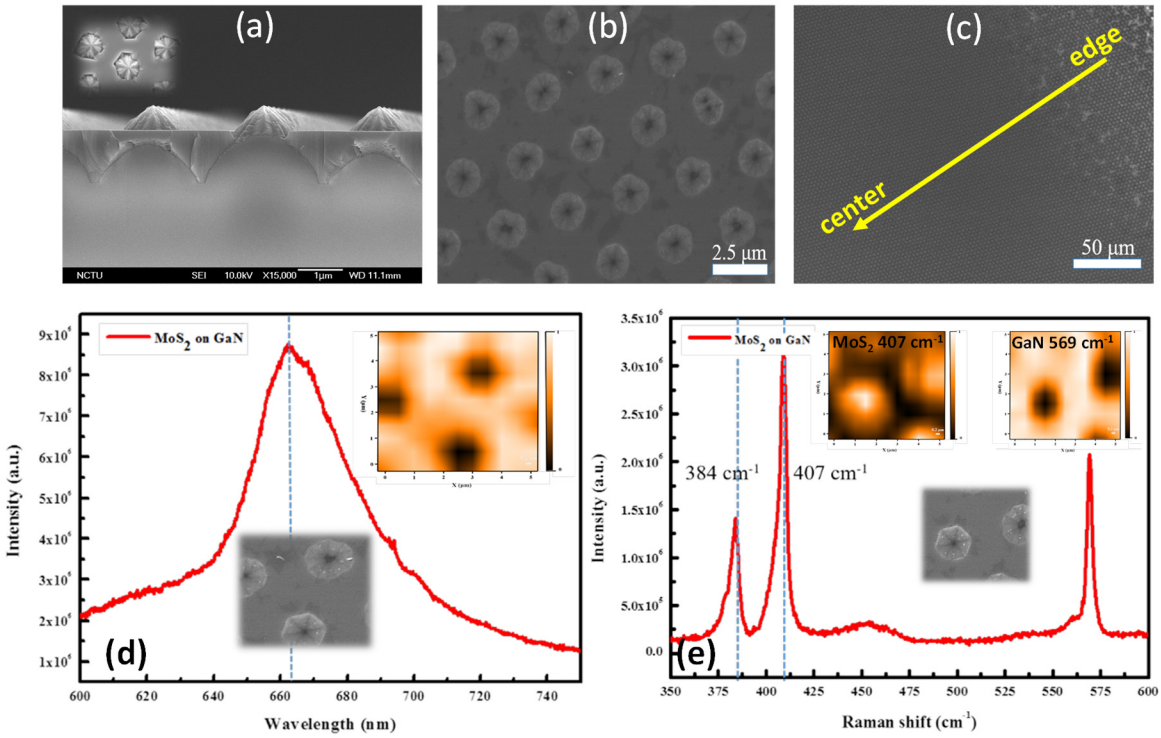

Figure 16: SEM images of (a) cross-section of patterned GaN structure with inset showing the top view; top view of MoS_2 grown on the GaN sample in (a); and (c) zoomed-out view of (b) all the way to the edge of a ~ 1 cm^2 size sample to show uniformity. (d) PL spectrum and map, showing stronger MoS_2 emission from the planar area; (e) Raman spectrum taken from the pyramid top and corresponding Raman mapping showing stronger MoS_2 signal on pyramids and stronger GaN in planar area.

Figure 16 shows the preliminary results on MoS_2 growth on patterned GaN substrates. The GaN pyramid array was grown on a patterned sapphire substrate as shown in Figure 16(a) (inset shows the top view image). The GaN pyramids show multiple crystal facets, including some rough sidewalls, while the area inbetween the pyramids show smooth surfaces. We achieved growth of MoS_2 across the entire GaN surface including both the planar area and the sidewalls of the pyramids [Figure 16(b)]. The MoS_2 coverage across the centimeter size sample is uniform except the very edges of the sample, which is shown in Figure 16(c). Spatially resolved Raman and PL characterization were performed. Strong PL was observed in the planar area while the pyramidal area showed near zero emission under the same condition, as seen in the PL spectrum in Figure 16(d) and mapping shown in the inset. However, much strong Raman signal originates from pyramid regions [Figure 16(e)] than the planar area (Raman spectrum in the planar region not shown). The A_{1g} peak is shifted by ~ +2 cm^{-1} for the pyramid area, possibly caused by the difference between the number of layers of MoS_2 in those two regions. Based on these observations, we believe that monolayer is formed in the planar GaN, in the same way MoS_2 was grown on unpatterned substrates, while multilayer MoS_2 is formed in the pyramid regions. Crystal

orientation dependence and surface roughness could both contribute to the difference in growth behavior.

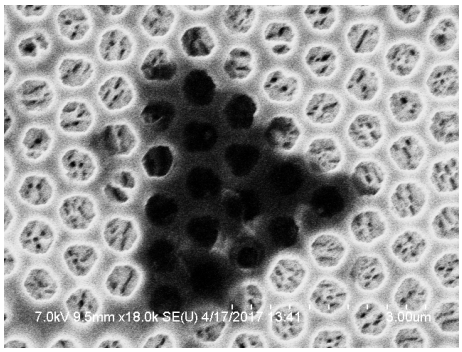

Figure 17: SEM of one MoS2 trigangular shaped flake on periodically perforated GaN substrate.

More relevant to the proposed monolithic integration of MoS_2 on photonic crystal resonator structure, we have also attempted to grow MoS_2 on GaN substrates with indentations. Shown in Figure 17 is our initial results on MoS_2 growth on periodically etched GaN substrate. The etching was done using metal-assisted chemical etching (MacEtch), which is an anisotropic wet etching without high energy ion induced damage. Although low in density, triangular shaped the MoS_2 flakes was observed across multiple shallow vias of GaN, as shown in Figure 17. Efforts are underway to improve the density and characterize the resulted film.

11. Development of 2D material preparation and integration processes (Zhou-Li-Fan groups, Year One)

Mechanical exfoliation of bulk crystals by tape is a well-known technique for producing high quality 2D material flakes. The downside is the low yield and the resulting monolayer flakes are typically under 10 μm for transition metal dichalcogenide (TMDC) due to inferior stiffness compared to graphene. Exfoliation using polydimethylsiloxane (PDMS) stamps, which can form conformal contact with 2D materials, has a better chance for larger flakes (tens of micrometers). However, the yield is still very low. Recently methods for large area exfoliation based on the strong bonding between gold and sulfur atoms were proposed [12, 13], in which gold is used as an intermediate layer in the exfoliation process. Based on the proposed methods and the well-established PDMS transfer printing technique at UTA, the process for gold-mediated exfoliation and transfer was developed.

Figure 18(a) shows the process flow of the technique: (1) Bulk MoS_2 or WSe_2 flakes are exfoliated from large crystals and deposited onto tapes. Only a few times of peeling is needed which results in flakes in large lateral sizes. (2) About 100 nm of gold are deposited on the bulk flakes using an AJA electron beam evaporator, as shown in Figure 18(b). (3) A piece of PDMS stamp, prepared with a 10:1 ratio of PDMS and curing agent, is brought into contact with the gold surface and peeled off rapidly. Gold and 2D material flakes are detached from the bulk crystal and remain on the PDMS stamp. Figure 18(c) shows the photograph of a PDMS stamp with WSe_2/gold flakes on top. The stamp is bonded to a fused silica carrier wafer to minimize the formation of wrinkles and ripples. The flakes on PDMS stamp are inspected under an optical microscope, where monolayer can be identified by color contrast. As in Figure 18(d), monolayer regions are marked by white dashed lines. There is a high chance to obtain monolayer 2D material

flakes with this method as the bonding between the topmost monolayer to gold is stronger than that to the underlying bulk crystal. (4) Having identified and recorded the position and shape of the monolayer flakes, the PDMS stamp is flipped over and brought into contact with the target substrate with the flakes facing down. Then the stamp is released slowly to leave the gold-coated flakes attached to the target substrate. In this step a Karl Suss MJB3 mask aligner, shown in Figure 18(e), is used for aligning the flake to the target cavity and monitoring the process of release. (5) The sample is baked at 70°C for improving adhesion. Then the gold layer is etched away in I_2/KI/DI water followed by a dip in solvents to clean the residue.

Figure 19(a) shows the optical microscope image of a heterostructure cavity sample integrated with an MoS_2 flake, with the monolayer region marked by dashed lines. A few of the heterostructure cavities are covered by monolayer MoS_2. This can be further confirmed under SEM inspection, shown in Figure 19(b)-(d). The contrast difference between the covered and uncovered areas are clearly visible.

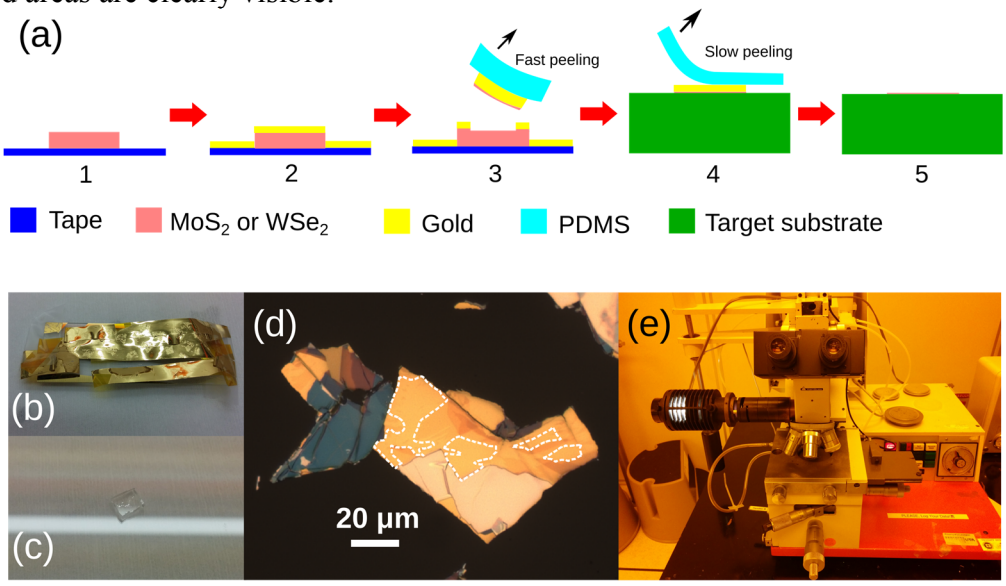

Figure 18: Gold mediated 2D material exfoliation and transfer process: (a) Sketch of the process flow. (b) Photograph of gold-coated bulk WSe_2 on tape. (c) Photograph of WSe_2/gold flakes on top of a PDMS stamp, corresponding to the result of step 3 in (a). (d) Microscope image of WSe_2/gold flakes on a PDMS stamp. The monolayer regions are marked by white dashed lines. (e) The Karl Suss MJB3 aligner used to align and transfer 2D material.

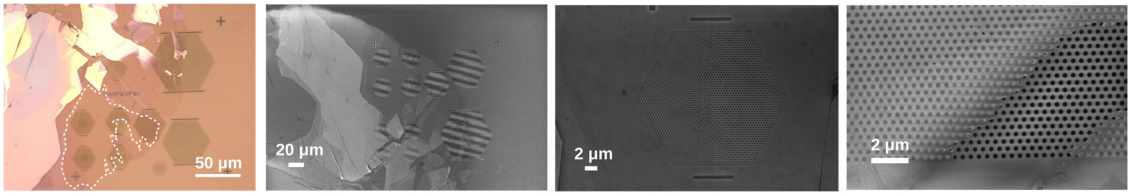

Figure 19: Aligned transfer of an MoS_2 flake on a heterostructure cavity sample. (a) Microscope image of the transferred sample. Monolayer regions are marked by white dashed lines. (b) SEM image of the same sample. (c) SEM image of a heterostructure cavity fully covered by monolayer MoS_2. (d) SEM image of the edge of the monolayer MoS_2 flake, showing the contrast difference of the areas with and without monolayer MoS_2 coverage.

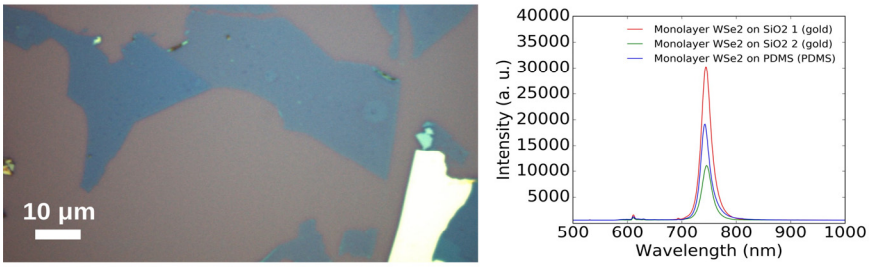

(a) (b)

Figure 20: Comparison of the emission of monolayer WSe_2 produced by gold-mediated exfoliation and PDMS exfoliation. (a) Optical microscope image of a WSe_2 flake on 285 nm SiO_2 on silicon. (b) Emission intensity of monolayer WSe_2 flakes by gold-mediated and PDMS exfoliation measured at the same conditions.

We compared the emission of the 2D materials by gold-mediated exfoliation and PDMS exfoliation. Figure 20(a) shows a monolayer WSe_2 flake on 285 nm SiO_2 on silicon substrate prepared by gold-mediated exfoliation. The emission of several flakes on the same sample were measured together with a monolayer WSe_2 flake on PDMS prepared by PDMS exfoliation in the same condition. The emission of 2D material is highly dependent on doping, substrate and strain. From the measured result in Figure 20(b) the emission between monolayer WSe_2 flakes prepared by both methods are comparable. However, we do notice that flakes prepared by the method developed generally have residue on top, which is visible in Figure 20(a). The origin of the residues and the possible impact to the cavity performance after transferring are still under investigation.

12. Emission enhancement of monolayer MoS_2 integrated on cavities (Zhou Group, Year One)

Based on the 2D material integration processes developed, we transfer-printed monolayer MoS_2 on the silicon nitride cavities which have been identified to have resonances within the emission spectrum. As shown in Figure 21. The cavity "A" is a large area defect free photonic crystal cavity. The cavity "B" is a lateral confined heterostructure cavity and the cavity "C" is a nanobeam cavity.

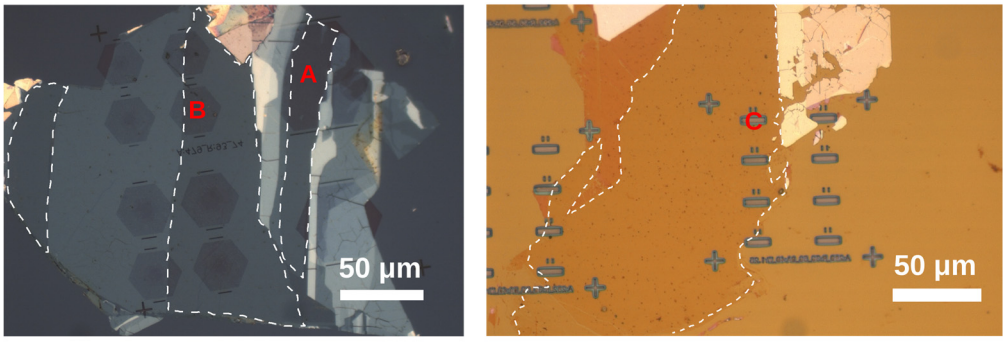

(a) (b)

Figure 21: Microscope images of monolayer MoS_2 integrated silicon nitride cavities: (a) Defect free and heterostructure cavities. (b) Photonic crystal nanobeam cavities. The monolayer areas are marked by white dashed lines.

The measurements were performed on a Thermo DXR Raman microscope with a 532 nm laser and a 400 g/mm grating. For the defect free and heterostructure cavities a 10×, 0.25 NA objective

lens was used to focus the excitation laser and collect the emission signal. An iris was installed at the back aperture of the objective lens to reduce the NA, as the configuration used in Section 7.b. For the nanobeam cavity a 100×, 0.9 NA objective lens was used.

Figure 22(a) shows the emission enhancement by the defect free 2D photonic crystal cavity. As the full size of the photonic crystal is around 70 μm, only part of it was covered by the monolayer MoS_2 film, which the spectrum was measured on. The measured emission spectrum is plotted as the red curve. Compared to the emission of monolayer MoS_2 measured on an unpatterned area on the same chip with the same excitation and detection conditions, an emission intensity enhancement of 2-folds is observed. And some peak features are visible which are absent in the off-cavity spectrum.

The blue curve in Figure 22(a) is the measured cross-polarized white light reflection spectrum of the same sample before MoS_2 integration, which shows resonance peaks of the defect free photonic crystal. Compared to the reflection spectrum, the peaks in the emission spectrum have similar features, and are red shifted and broader, which are due to increasing refractive index and loss by the presence of monolayer MoS_2.

Figure 22(b) shows the emission spectrum of a heterostructure cavity fabricated on the same chip. Compared to the emission of off cavity MoS_2, the on-cavity emission also has a 2-fold enhancement. Apart from that, a series of peaks resemble that of the multiple order heterostructure cavity modes can be observed. As stated in Section 7.b, the incorporated lateral confinement results in improved quality factor and field concentration, which contributes to the emission enhancement. A fitting of the fundamental mode is plotted in the inset of Figure 22(b). The fitted quality factor is 735, also limited by the loss introduced by MoS_2.

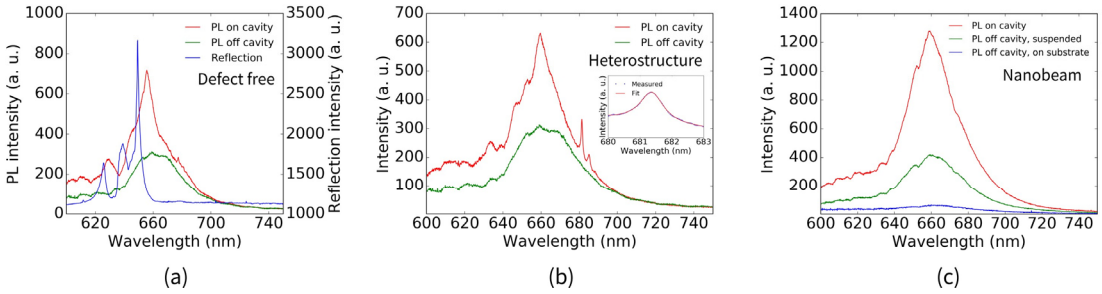

Figure 22: Measured monolayer MoS_2 emission enhancement by cavities: (a) Defect free 2D photonic crystal. (b) Heterostructure cavity. (c) Nanobeam cavity.

For the nanobeam cavity shown in Figure 21(b). The measured emission spectrum plotted in Figure 22(c) shows a 20-fold enhancement compared to monolayer MoS_2 on unpatterned silicon nitride surface on the same chip. However, as the emission of MoS_2 is highly dependent on substrate, it is expected that suspended MoS_2 film has stronger emission than unsuspended one. We also measured the emission of suspended MoS_2 on an unpatterned trench. The emission on cavity still shows a 3-fold enhancement. In contrast to heterostructure cavities, we did not find peak features in the emission spectrum of nanobeam cavities, despite that the overall enhancement factor is larger. This may due to the emission from the cavity mode is embedded within the background fluorescence peak since the width of the waveguide that forms the nanobeam is around 400 nm while the spot diameter of the pump laser is 2.1 μm, thus suspended MoS_2 at off-cavity area is also excited.

In conclusion, we have demonstrated emission enhancement of monolayer MoS_2 integrated on silicon nitride cavities. No lasing was observed from these devices yet. We have planned the

following to identify and overcome the limitations: (1) Characterize the loss from 2D material films, including absorption and scattering losses. It seems the material properties (especially index and absorption coefficient of mono- or few- layer 2D materials are largely dependent on the preparation method and surface/interface conditions. Precise determination of these parameters is crucial towards high quantum efficiency emission and high energy efficiency lasing. (2) Improve the emission of 2D materials, including performing surface passivation [14], plasma treatment [15], h-BN buffering [16] and switching to high quantum yield materials such as WSe_2 and WS_2. (3) Improve the field overlap in the 2D material film by incorporating encapsulation and modifying cavity design for more evanescent components. (4) Investigate the emission at lower temperatures. Additional collaborations are being established with 2D Crystal Consortium at PSU, a Materials Innovation Platform funded by NSF, to leverage material advances and to address some of device integration related challenging issues.

13. Optical pumped lasing action from 2D-Heterostructure PhC cavities (Zhou-Fan-Li, Year Two)

In year one we have demonstrated MoS_2 PL modification by heterostructure PhC cavities and showed that the cavity resonance features can be detected in the PL spectrum. Based on those we have continued to optimize in the cavity configuration and realized potential lasing action from such cavities with optical pumping. The improvements we have made are as follows: (1) We have changed the gain material from monolayer MoS_2 to monolayer WS_2, which has higher quantum yield than MoS_2 at room temperature. In Figure 23(a) the PL spectra of exfoliated WS_2, WSe_2 and MoS_2 at the same excitation and measurement condition are plotted. Even compared to suspended MoS_2, which has superior properties than supported due to relaxed strain and no substrate-induced doping, the WS_2 on SiO_2 substrate is still nearly 80 times brighter. WS_2 also has brighter emission than WSe_2 and is more compatible with the gold-assisted exfoliation method due to the strong bond between sulfur and gold atoms. (2) The thickness of the silicon nitride layer has been reduced from 160 nm to 112 nm, accommodating to the shorter emission wavelength of WS_2 and increasing the confinement factor. (3) A thin layer of fluoropolymer (CYTOP CTL-809M) was coated on top of the sample after the monolayer WS_2 transfer printing process for providing protection and improved confinement factor.

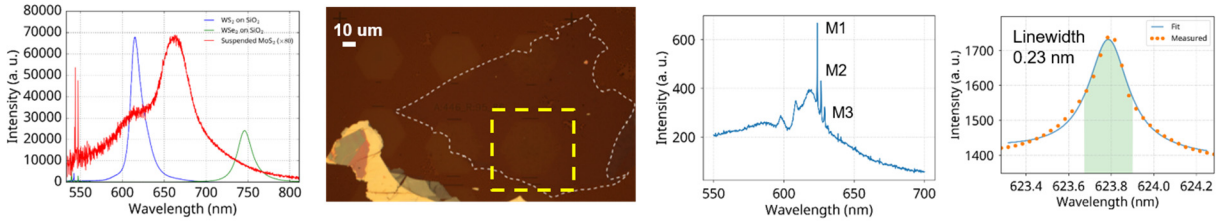

Figure 23 Heterostructure PhC cavities integrated with monolayer WS_2. (a) Comparison of PL intensities from monolayer WS_2, WSe_2 and MoS_2 excited at the same condition. (b) Microscope image of the fabricated device. The cavity under consideration is marked by the yellow dashed square and the monolayer region is marked by white dashed lines. (c) PL of the cavity when pumped at the center of the core region with 150 μW of power on sample. The multiple cavity resonances are designated by M1, M2 and M3 respectively. (d) Lorentzian fitting of the peak M1.

Figure 23(b) shows the microscope image of the sample where the monolayer WS_2 is marked by white dashed lines and the cavity under consideration is in the yellow dashed square. The device is pumped by a 445 nm laser focused at the center of the core region. The focused pump laser spot has an elliptical shape and the measured FWHM beam widths are 3.6 μm in the major axis and 2.5 μm in the minor axis. The measured PL spectrum at 150 μW pump power is plotted in Figure 23(c), where the PL of monolayer WS_2 is strongly modified by the cavity resonances. Three sharp peaks, corresponding to the multiple resonance modes of the cavity are denoted by "M1", "M2" and "M3" in the following analysis, with "M1" being the dominating fundamental mode. A Lorentzian fitting of M1 results in a linewidth of 0.23 nm [Figure 23(d], or a Q factor of 2,700.

The passive cavity mode structures are presented in Figure 24. Before the integration of monolayer WS_2, the resonant modes can be probed by measuring the enhanced fluorescence of silicon nitride. In Figure 24(a) we can see the three peaks resembling those from Figure 23(c). The symmetry-induced degeneracy of the higher order modes M2 and M3 are broken by the errors introduced in fabrication, which caused the slight splitting of these two modes. The Lorentzian fitting of M1 in Figure 24(b) shows a linewidth of 0.07 nm, or Q around 8,000. After finishing the device by the integration of monolayer WS_2 and spin-coating of the fluoropolymer layer, the cold cavity features were measured by cross-polarized white light reflection. In Figure 24(c) and (d) the resonances show a red shift and broader linewidth, which is due to the increased absorption and scattering by the presence of monolayer WS_2. When pumped, the linewidth of M1 in Figure 23(d) is significantly narrower than the passive case in Figure 24(d), indicating the effect of increased gain of monolayer WS_2.

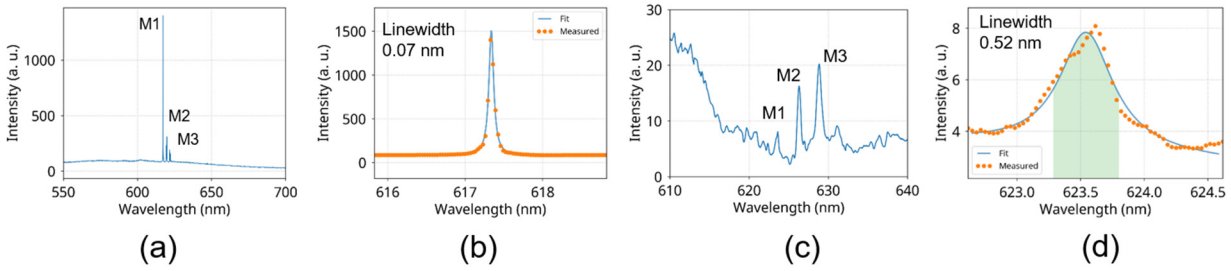

Figure 24 Passive properties of the cavity. (a) PL of the silicon nitride cavity before WS_2 integration. (b) Lorentzian fitting of the mode M1. (c) Cold cavity resonances after WS_2 integration measured by cross-polarized reflection. The modes show a red shift and broader linewidths. (d) Lorentzian fitting of the mode M1.

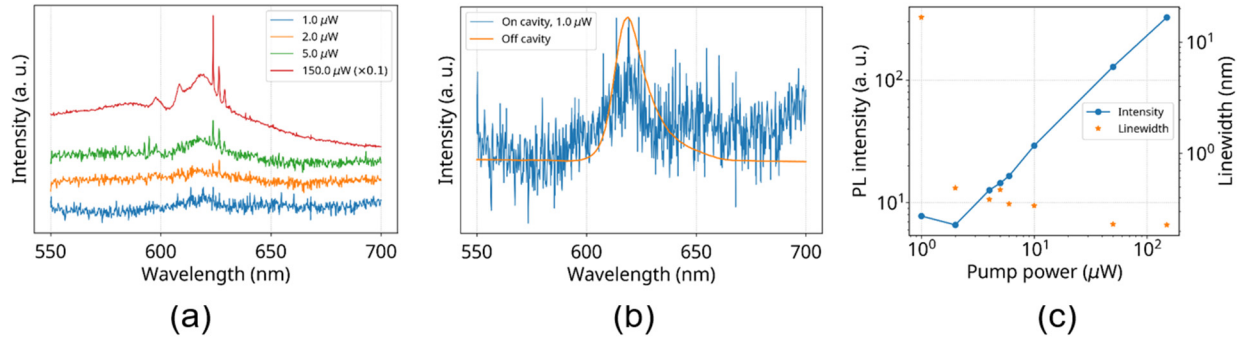

Figure 25 Power dependent PL characterization of the cavity. (a) PL spectra at different pump power on sample. The positions of the curves are shifted in the vertical direction for clarity. (b) Comparison of the PL at 1 μW to the spontaneous emission of WS_2 measured from off-cavity position. (c) L-L curve of the mode M1 in log scale.

We measured the pump power dependent PL of the device, shown in Figure 25(a). At 1 μW pump power only the envelop of the spontaneous emission of WS_2 is visible. As the pump power increases the cavity modes starting to show up and eventually the mode M1 dominates the PL spectrum.

To verify whether the measured PL at 1 μW is purely from spontaneous emission of WS_2, we normalize and compare it with the PL from off-cavity WS_2 in Figure 25(b). Although the on-cavity emission is noisy due to the limitation of our detector, we can still see the envelop of the WS_2 PL that resembles the off-cavity case, while the cavity features are indistinguishable. Therefore, in the L-L curve in Figure 25(c) we use the linewidth of the whole spontaneous emission peak for the pump power at 1 μW, and use the Lorentzian fitted linewidth of the cavity resonance peaks for higher pump powers where the peak feature is more profound.

We summarized, to our best knowledge, the results of our potentially lasing device in Table 3, with the estimations listed in the footnotes. And the existing works on 2D lasers are also listed for comparison. Due to the limitation of sensitivity of our detector and low signal level, the SNR at the pump power where the cavity peak starts to emerge is low, which prevents us in obtaining a clear threshold behavior. However, the linewidth we have obtained at higher pump powers is comparable to the existing works on TMDC based lasers and the dominance of the resonance peak is also encouraging. We are working on further improving the quantum yield of the gain material which would result in a better signal level and enable the possibility to obtain a far field emission pattern from the cavity experimentally. And the $g^{(2)}$ measurement, which would provide a decisive proof of coherence, is also being explored.

Table 3 Performance comparison with 2D lasers reported so far

Cavity type	PhC L3[17]	Disk[18]	Disk & sphere[19]	PhC nanobeam[20]	Heterostructure PhC (This work)
Cavity material	GaP	Si_3N_4 / SiO_2	SiO2	Si / PMMA	Si_3N_4
Gain material	1L WSe_2	1L WS_2	4L MoS_2	1L $MoTe_2$	1L WS_2
Temperature	<160 K	10 K	RT (N_2 ambient)	RT	RT
λ (nm)	740	612	630~700	1132	623.8
Q_{exp}	2465	2604	3000	5603	2700
Γ (%)	-	0.11	0.1	0.0145	[a]0.1
Pump	632 nm CW	473 nm fs	514 nm CW	633 nm CW	445 nm CW
Threshold power	27 nW	-	5 μW	97 μW	[b]1 ~ 2 μW
Threshold power density	1 W / cm^2	5~8 MW / cm^2	-	6.6 W / cm^2	[c]14 ~ 29 W / cm^2
Threshold modal gain (cm^{-1})	-	78.8	39	51	[d]60
Threshold gain (cm^{-1})	-	71636	3900	3.5e5	[d]60249
Footprint (μm^2)	36	8.55	177	2.6	1292

a: Estimated by FDTD simulation of the mode of the core region PhC at Γ. Monolayer WS2 is not modelled.
b: Estimated from the onset of the resonance peak in the power dependent PL spectra.
c: Assuming an elliptical beam with major and minor axes of 3.6 μm and 2.5 μm respectively.
d: Radiation loss estimated by considering a defect free PhC identical to the core region $\alpha_r = 4\pi/(\sqrt{3}aQ)$

14. Selective emission quenching and potential gain/loss modulation of CVD WSe_2 (Zhou-Fan group, Year Two)

For realizing the concept of gain/loss modulation in 2D TMDC. We developed a method to selectively quench the exciton emission by SiO_2 lift-off. The material we are using is CVD grown monolayer WSe_2 grown on sapphire substrate from PSU. A layer of PMMA (~400 nm) is first spin-coated on top of the WSe_2 as carrier and a PDMS stamp is then attached to PMMA for handling. The chip is then immersed in DI water. With gentle stirring or ultrasonic agitation, water would penetrate between PMMA and sapphire and release the WSe_2 film in the process since both PMMA and WSe_2 are hydrophobic and sapphire is hydrophilic. The released WSe_2, together with the PMMA carrier is then transfer-printed on silicon nitride substrate. After patterning the PMMA film with EBL, a thin (~ 10 nm) layer of SiO_2 is deposited by sputtering and lift-off.

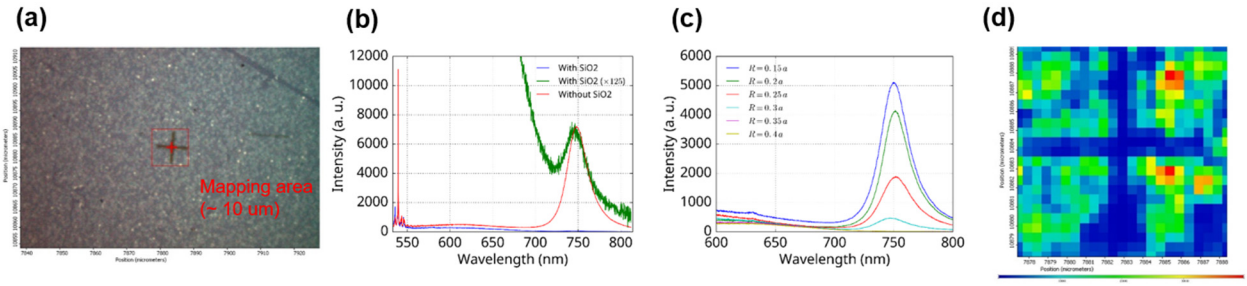

Figure 26 Selective emission quenching of monolayer WSe_2. (a) Lift-off SiO_2 patterns on monolayer WSe_2. (2) Comparison of the WSe_2 emission with or without SiO_2 deposition. The emission intensity has been suppressed by two orders of magnitude. (c) PL from SiO_2 rod arrays on WSe_2 with different filling factors. (d) PL mapping of the area in (a) marked by the red square.

Figure 26(a) shows the microscope image of SiO_2 patterns on CVD WSe_2. The red square indicates the area around the cross mark for PL mapping. We measured the PL of WSe_2 with and without SiO_2 deposition and plotted them in Figure 26(b). With the deposited SiO_2 the exciton emission form WSe_2 is suppressed by two orders of magnitude.

The gain/loss modulation concept requires the gain and loss materials to be arranged into a periodic structure. To verify the effect of filling factor to the emission quenching we fabricated SiO_2 rod arrays with various radius. The lattice constant of the rods was fixed to be 500 nm. Figure 26(c) shows that the intensity of emission drops with increasing radius of the rods. The PL map over the square area in Figure 26(a) is plotted in Figure 26(d), the low emission intensity at the cross mark indicates the quench is indeed caused by the deposition of SiO_2.

In conclusion we have demonstrated it is viable to selectively quench the emission of monolayer WSe_2 by sputtering deposition of a thin layer of SiO_2. In the next phase we will be working on characterizing the gain and loss properties of WSe_2 under such treatment and demonstrating the band structure of periodic gain/loss materials.

15. Confirmation and direct far field pattern measurement of the WS_2 PCSEL (Zhou group, Year Three)

In year two we have a preliminary demonstration of an optical pumped PCSEL based on monolayer WS2 which showed linewidth narrowing compared to the cold cavity case. During year three, we focused on improving the design and process to obtain reproducible and more conclusive results. Clear linewidth narrowing and threshold behavior were demonstrated. The far field radiation pattern from the lasing device was experimentally measured which agreed with the theoretical prediction. Efforts were also devoted to exploring the lifetime and coherency properties of the WS2 PCSEL devices.

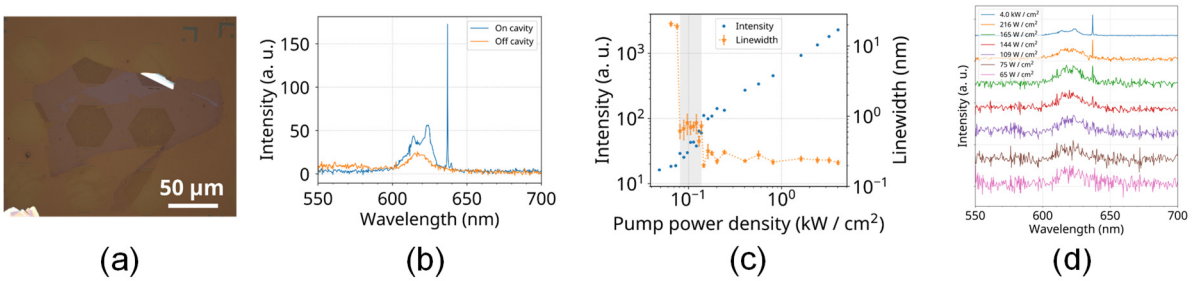

Figure 27 Confirmation of the WS2 PCSEL. (a) Microscopy image of the fabricated devices. (b) Measured PL spectra on and off the PhC cavity. (c) Measured L-L curve and linewidth. A clear threshold behavior was observed. (d) Power dependent PL spectra at lower pump power densities.

A total of 6 working devices from 4 sample runs have been fabricated and characterized. Figure 27 shows the measured data from a representative device. From the power dependent PL spectra in Figure 27(d), at lower pump power densities the device only shows a broad spontaneous emission envelop with a disappearing cavity resonance feature due to low SNR. With the increasing of pump, the resonant peak emerges and eventually dominates the spectra. In the L-L curve shown in Figure 27(c) a soft but clear kink can be observed together with a clear linewidth narrowing over two orders of magnitude.

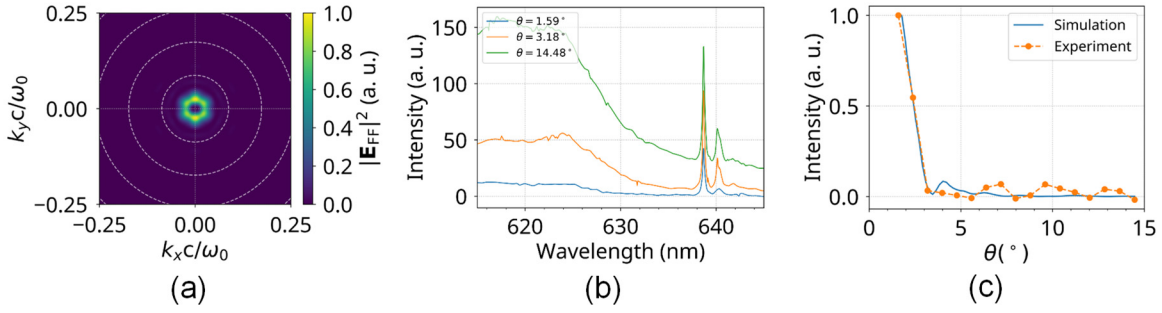

Figure 28 Direct measurement of the far field pattern from the WS2 PCSEL. (a) Simulated far field pattern of the resonant mode. (b) Above-threshold PL spectra collected at various collection angles. (c) Measured and simulated far field profiles in the collection angle.

As the designed device has intrinsically surface-emitting property, we carried out a far field beam measurement to demonstrate that. The theoretical far field pattern was first calculated

through a near-to-far transformation based on the FDTD simulated near field profile. In Figure 28(a) the white dashed circles indicate polar angles in 5° steps. Therefore, the far field emission is expected to be concentrated in a few degrees. We used an iris placed in the infinity space of the micro-PL setup to restrict the angle of collection and profile the far field. Plotted in Figure 28 are the PL spectra of the device with varying collection angle θ. As θ decreases, the intensity of the cavity resonance reduces much slower than the background, indicating that the emission from the cavity resonance concentrates near the surface-normal direction. By collecting the spectra at different θ and performing a central difference on collected peak intensities in respect to θ, we are able to obtain a directly measured far field emission profile in polar angle. Figure 28(c) shows that the measured and simulated far field profiles agree very well.

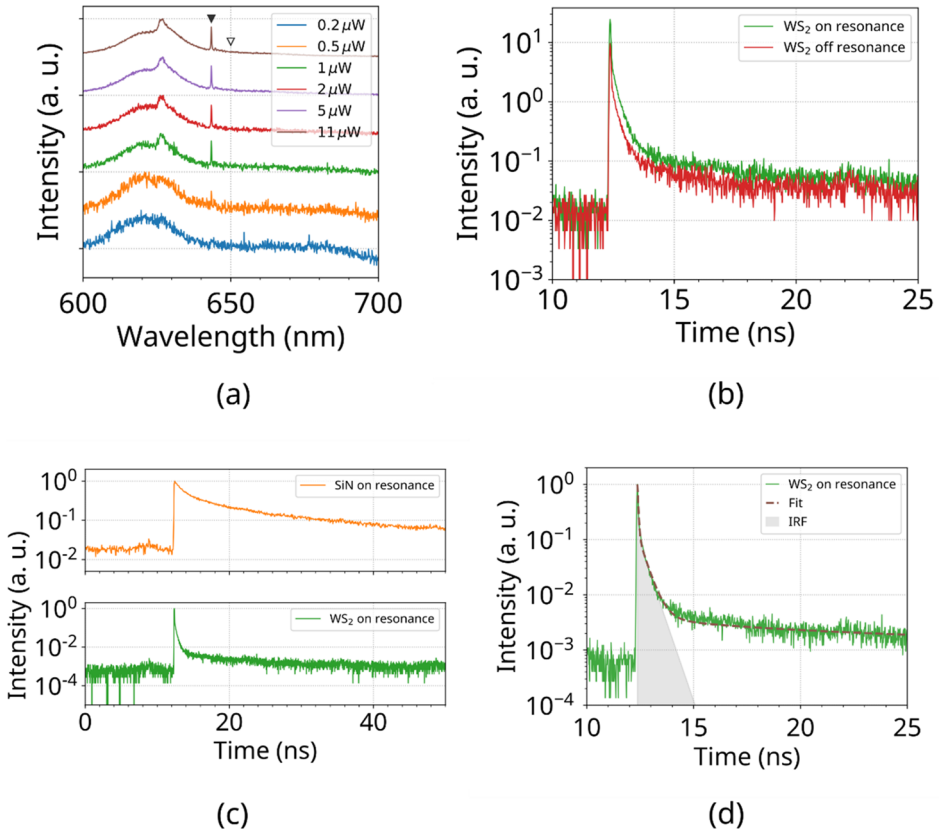

Figure 29 Time resolved PL of the WS2 PCSEL. (a) Power dependent PL of the device under test, showing lasing behavior. (b) TR PL of WS_2 at on/off resonance wavelengths. (c) Comparison of lifetimes between emission from WS_2 and SiN. (d) Fitting of the lifetime of on resonance WS_2 emission.

Due to the defects and impurities in the LPCVD silicon nitride, a broadband fluorescence can be defected from SiN itself. And cavity-enhanced fluorescence was also used for characterizing the passive resonance before the integration of monolayer WS_2. The low absorption loss of SiN and the high *Q* cavity design result in a strong and prominent cavity feature on the SiN emission spectra. After the integration of WS_2, one may question whether the sharp resonance feature is from WS_2 or SiN. To investigate this matter, we collaborated with the University of Texas at Dallas for a time resolved PL measurement. Another PCSEL sample was prepared which shows similar behavior when pumped with a 400 nm picosecond pulsed laser (Figure 29(a)). The decay lifetime was then measured for the following cases: (1) WS_2 on resonance;

Solid triangle in Figure 29(a). (2) WS_2 off resonance; Open triangle in Figure 29(a). (3) SiN on resonance; A passive device on the same sample without WS_2. Comparing the absolute intensities of the on/off resonance emission in Figure 29(b), it can be seen that the increasing of emission is mostly contributed by the fast-decay component. And from the comparison of the lifetimes of WS_2 and SiN (Figure 29(c)) it can be concluded that the decay of the emission of WS_2 is much faster than that of SiN. To be specific, the lifetime of WS_2 is in the order of picoseconds, while that of SiN is in the order of nanoseconds. In Figure 29(d) we fitted the decay with a sum of two exponential and one stretched exponential functions. It is found that the primary fast-decaying component is limited by the instrument response function (gray shade). As we were measuring at high pump power which inverses WS_2, the decay lifetime is indeed short. By comparing the relative strengths of each decay component, we have found that the fast components (picoseconds) compose 99.4% of the total emission while the contribution from the slow component (nanoseconds) is only 0.6%, which unambiguity shows that the emission is mainly coming from WS_2.

16. Engineering of the far field pattern of the heterostructure PhC cavities (Zhou-Fan groups, Year Three)

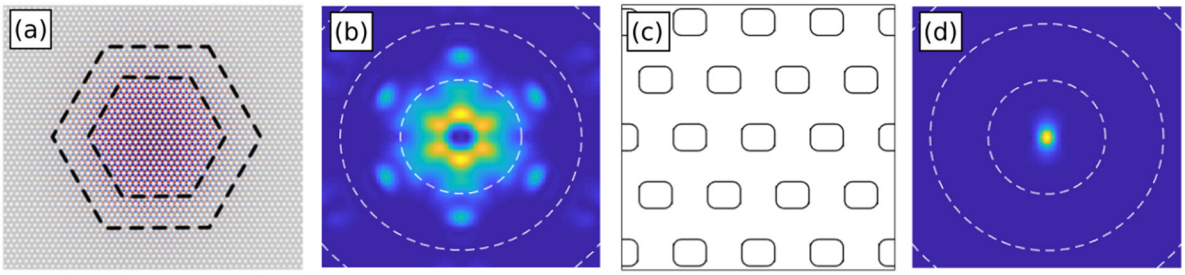

Figure 30 (a) Photonic crystal heterostructure cavity for single-sheet active material lasing. (b) Far-field emission profile of the cavity. The white dashed circles denote emission angle of 5, 10, and 15 degrees, respectively. (c) We introduce holes in the shape of rounded rectangles to break the point-group symmetry that ensures zero emission at zero angle. (d) This results in a very narrow, Gaussian emission profile with a maximum in the vertical direction.

In a recent paper (Ge et al., Appl. Phys. Lett. 112 141105 (2018)), we introduced a photonic crystal heterostructure cavity in a silicon nitride slab on quartz, optimized for a high quality factor despite the low refractive index contrast between the slab and the cladding. The purpose of this design is to be integrated with a signle-sheet 2D material to form a compact, low-threshold laser. An extra advantage of the design is that the far-field emission of the resonator is well localized within a small angle around the vertical direction (Figure 30(b)). Despite this, however, the far field has a node at exactly zero angle, because the heterostructure is constructed on the basis of a photonic crystal band with a dark mode at $k = 0$. Our published design thus does have the advantage that all of the emitted light can be collected with a small numerical aperture, but an even better design would have a narrow, Gaussian far-field profile with a peak at zero vertical angle. We have found that this can be achieved by fine-tuning the holes of the photonic crystal heterostructure. Specifically, by introducing holes in the shape of rounded rectangles (Figure 30(c)), we break the C6v point group symmetry which ensures the dark mode at $k = 0$. The rounded corners were introduced to match what is experimentally accessible, as sharp edges cannot be fabricated. By fine-tuning the two side-lengths of the rectangles, we designed a cavity with a theoretically predicted Gaussian emission profile centered at the vertical direction (Figure 30(d)).

17. Lasing in synthesized monolayer WS_2 (Zhou group, Year Three)

While we have demonstrated PCSELs using exfoliated monolayer WS2, the yield and achievable size of the exfoliated flakes are still limited despite an improved method being utilized. The aim of scaling of the output power and any practical application also calls for the large synthesized monolayer films. To explore the possibility of our cavity design on synthesized monolayers, we further collaborated with Penn State University for the wafer-scale MOCVD-grown monolayer WS_2, MoS_2 and WSe_2. Figure 31 shows the PL characterization of the MOCVD WS_2. Comparing with exfoliated monolayers, the as-grown synthesized film on sapphire shows considerably lower emission, which is expected since the synthesized monolayer is polycrystalline, and the density of defects would be higher than the monocrystalline exfoliated monolayers. We decomposed the PL spectrum of the MOCVD WS_2 into the sum of three Lorentzian functions, which correspond to the emission from exciton, trion and defects, respectively. In Figure 31(b), the emission from the defect state shows a significant contribution to the shoulder of the total emission above 650 nm, which, as will be presented below, have stronger coupling with the cavity resonance than that from the exciton and trion.

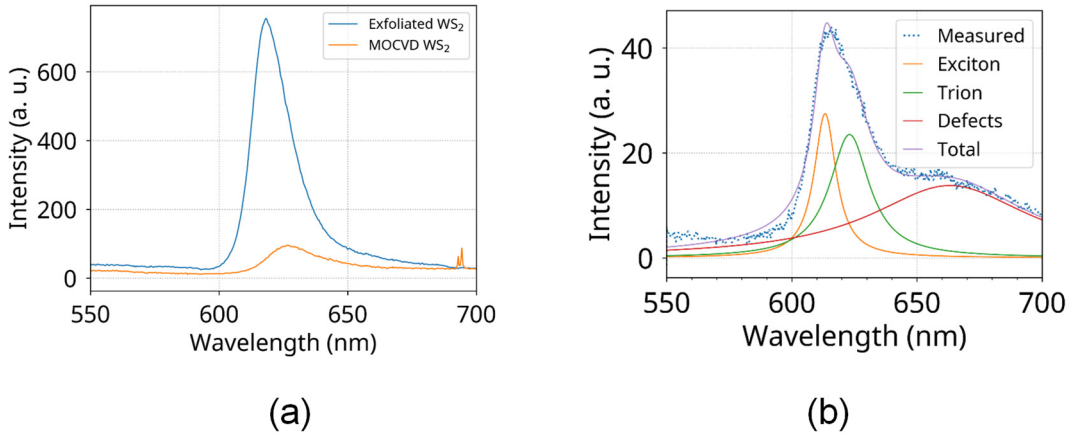

Figure 31 PL of MOCVD synthesized monolayer WS2. (a) Comparison of PL from exfoliated WS_2 on SiO_2 and as-grown WS_2 on sapphire. (b) Decomposition of the PL from MOCVD WS_2, showing a significant amount of defect emission.

Based on our previous effort in handling exfoliated TMDCs, we developed a water-based method for releasing and transferring synthesized TMDC. As the sapphire substrate that the TMDC is grown on is more hydrophilic than the SiO_2 substrate we used for exfoliated flakes, and generally no alignment is required for the large area film, the overall process is much simpler and has the potential in practical applications. The PMMA film is firstly spun-coated onto the TMDC and baked to form a carrier for mechanical support during releasing. It can also act as a buffer layer between the TMDC and PDMS to reduce contamination. The PDMS stamp on a glass handler is then attached to the PMMA and the full stack is immersed into DI water. After a brief ultrasonication, water penetrates between the TMDC film and sapphire which releases the film from substrate. The release film can be transferred onto the target by either transfer-printing or heating. To protect the TMDC from exposure to oxygen and water,

after removing the PMMA carrier and drying the film, we coated a layer to CYTOP as encapsulation.

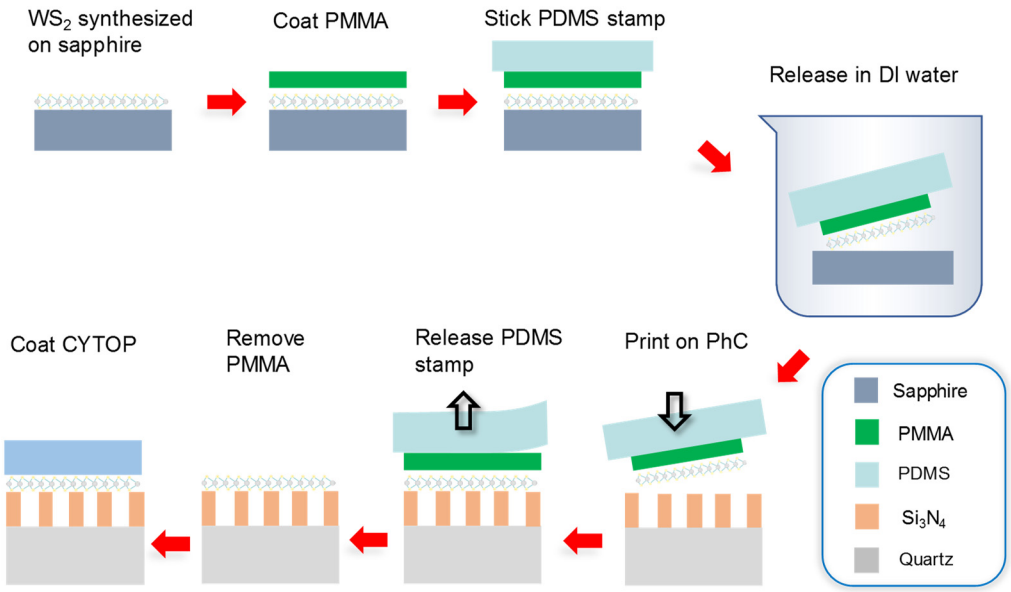

Figure 32 Processing flow of integrating large area synthesized WS2 onto SiN PhC cavities.

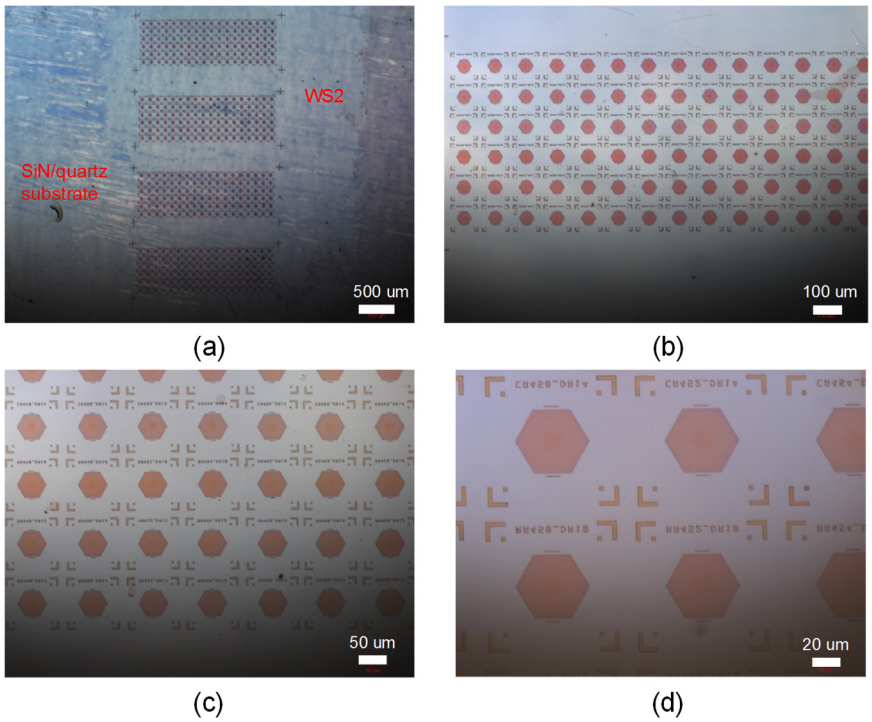

Figure 33 Microscopy images of synthesized WS2 integrated on PhC arrays at different magnifications.

Combining the improved heterostructure PhC cavity design and the release-transfer method, we fabricated PCSEL samples using synthesized monolayer. **Error! Reference source not found.** shows the microscopy images of the large area film integrated onto the PhC cavities and Figure 34(a) is the SEM image of the PCSEL cavity with a rectangular air hole. After the integration of WS_2, the devices were pumped at room temperature using a 450 nm laser diode operated in quasi-CW mode (100 ns width, 10% duty cycle). Features corresponding to the cavity resonances can be clearly identified in Figure 34(b) compared to off-cavity WS_2. And the high Q fundamental mode dominates the emission spectrum. Power dependent PL measurement shows the narrowing of the linewidth of the fundamental mode with increasing pump power, which is similar to the results obtained in exfoliated flakes (Figure 34(c)). The uniform large area monolayer enables the systematic study of the coupling of the WS_2 emission to cavity modes at different wavelengths as the resonance can be easily and robustly tuned through changing the lattice constant, while the linewidths stay similar. By tuning the resonance over the emission spectrum of synthesized WS_2, it was observed the coupling of the emission to the cavity mode is the strongest when the resonance matches the emission from the defects (Figure 34(d)), which is of striking difference compared to the exfoliated flakes. Further investigation on the underlying physics is still being carried out.

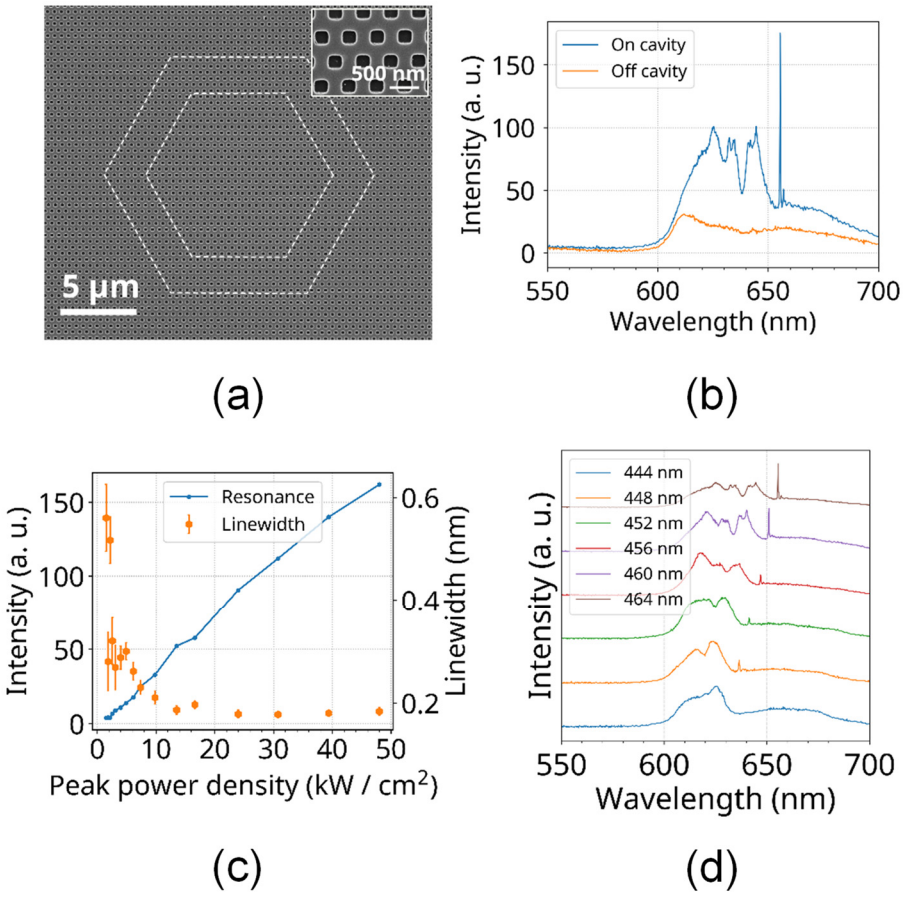

Figure 34 PCSEL based on synthesized WS2. (a) Fabricated SiN heterostructure PhC cavity before WS2 integration. (b) Measured PL on and off the cavity. (c) Measured L-L curve and linewidth. (d) Resonant wavelength tuning by varying the lattice constant.

18. 2D material transfer-printing on an automatic assembly platform (Zhou group, Year Three)

Based an automatic assembly platform at UTA (FiconTEC FL-200, shown in Figure 35(a)), we built an improved transfer-print system which greatly enhances the capability and yield of 2D material handling. A home-built transfer microscope was mounted on the system which provides colored imaging for 2D materials. And the robotic arm of the system was utilized as the PDMS stamp holder for its accuracy, stability and wide tunable range of speed. During the releasing phase of the transfer-print process, the robotic arm (i.e. the PDMS stamp) is programmed to raise in 100 nm steps and hold in between the steps to allow the stamp to be slowly released. Compared to manual transfer-printing using our previous aligner-based setup (Figure 19) or a manual XYZ stages, the automatic transfer-printing tool has much higher yield for winkled films, and is capable to reliably release large area films in duration of hours.

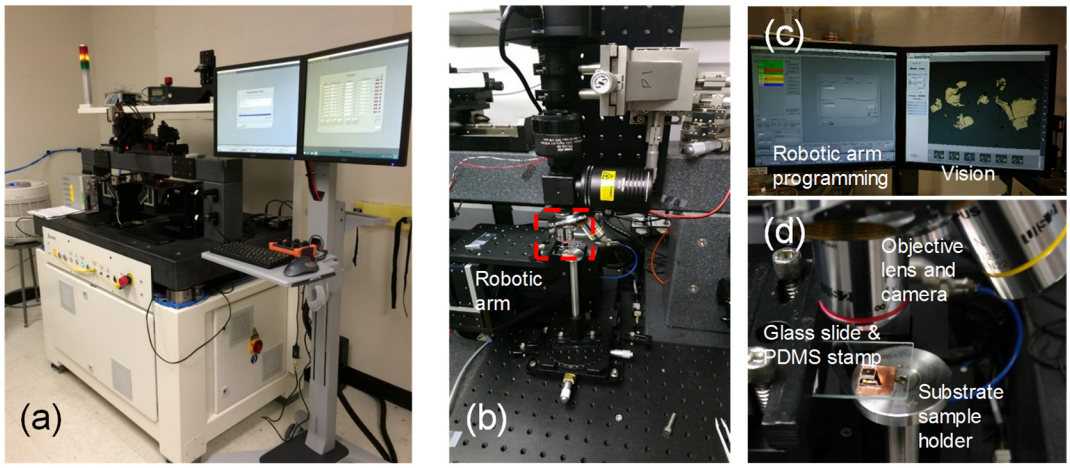

Figure 35 Transfer-printing system based on the FiconTEC assembly platform. (a) The assembly platform before modification. (b) Home-built transfer microscope. (c) Monitors displaying the programming interface and camera vision. (d) Close-in view of the PDMS stamp and the target substrate.

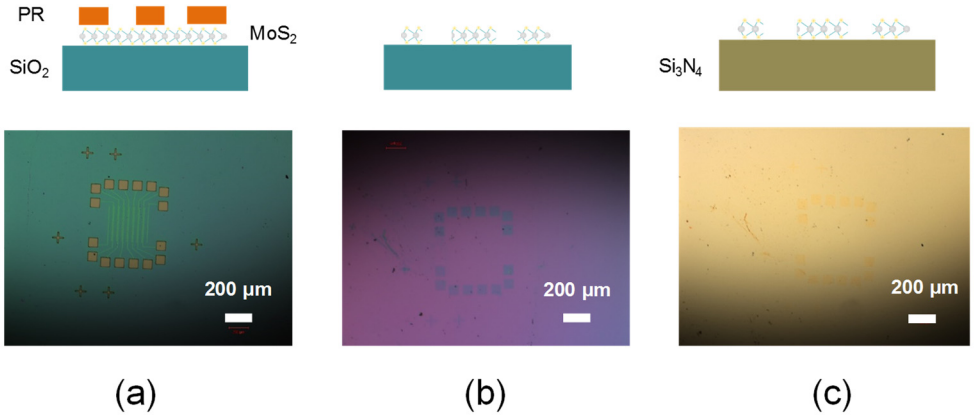

Figure 36 Demonstration of transferring patterned 2D material on FiconTEC. (a) Photolithography patterns. (b) Patterned monolayer MoS_2 on SiO_2 substrate. (c) Patterned monolayer MoS_2 transferred onto Si_3N_4 substrate.

To demonstrate the capability of the system and exploring the possibility in large scale integration, we performed trial runs of transferring of patterned large area synthesized TMDC film. As shown in Figure 36, synthesized monolayer MoS_2 was first patterned by photolithography followed by oxygen plasma RIE. The patterned monolayer MoS_2 was then released by the water penetration method as stated in Section 17. Using the automatic transfer-printing system, the large area patterned MoS_2 was successfully printed on the target Si_3N_4 substrate. This demonstration shows our capability of assembling 2D materials or other nanostructures with high yield, accuracy and minimal manual intervention.

19. Publications

1. A. Cerjan and S. Fan, "Achieving Arbitrary Control over Pairs of Polarization States Using Complex Birefringent Metamaterials," Phys. Rev. Lett. **118**, 253902 (2017).
2. A. Cerjan and S. Fan, "Effects of non-uniform distributions of gain and loss in photonic crystals", *New Journal of Physics*, 18(12):125007, 2016.
3. A. Cerjan and S. Fan, "Eigenvalue dynamics in the presence of nonuniform gain and loss", *Physical Review A*, 94(3):033857, 2016.
4. W. D. Zhou, Y. Liu, X. Ge, X. Li, and S. Fan, "Approach total absorption in critically coupled photonic crystal structures with monolayer 2D materials (Invited)", META'16, the 7th International Conference on Metamaterials, Photonic Crystals and Plasmonics, Convention & Exhibition Centre, Torremolinos (Malaga), Spain, July 25, 2016 – July 28, 2016.
5. W. Zhou, S. Liu, D. Zhao, H. Yang, Z. Ma and M. Hammar, "Printed photonic crystal membrane lasers on silicon", *Asia Communications and Photonics Conference 2016*, AS1F.1, 2016.
6. W. D. Zhou, Y. Sun, Z. Ma,L. Menon, Y. Liu, H. Yang, and D. Zhao, "Hybrid Flexible Membrane Multi-Band Imagers and Optical Membrane Sensors (Invited)", *Symposium BM5: Materials for Bio-integrated Photonic Systems, MRS 2016 Fall Meeting, Nov. 27-Dec. 2, 2016,* Boston, Massachusetts, USA.
7. W. D. Zhou, S. Liu, D. Zhao, H. Yang, Z. Ma, and M. Hammar, "Hybrid Photonic Crystal Membrane Lasers on Silicon (Invited)", Photonics West, San Francisco, Jan. 28-Feb. 2, 2017.
8. W. D. Zhou, D. Zhao, H. Yang, and Z. Ma, "Fano Resonance Photonic Crystals for 3D Integrated Photonics (Invited)", *OSA Integrated Photonics Research, Silicon and Nano Photonics (IPR) conference*, July 24-28, 2017, New Orleans, Louisiana, USA.
9. K. Jung, C. Liu, J.D. Kim, W. Choi, J. Fraiters, W. Zhou, H. Kuo, and X. Li, "Large Area MoS2 van der Waals Epitaxy on III-Ns and the Epitaxial Formation of a n-MoS2/p-InGaN Diode", IEEE Photonics Conference, Waikoloa, Hawaii, USA, Oct. 2-6, 2016.
10. C. Liu, K. Jung, W. Choi, J. Kim, M. Kim, X. Ge, H. Kuo, W. Zhou, and X. Li, "Large Area van der Waals Epitaxy of MoS2 on III-Nitride Substrates", MRS-Spring 2017.
11. W. D. Zhou, D. Zhao, H. Yang, and Z. Ma, "Fano Resonance Photonic Crystals for 3D Integrated Photonics (Invited)", *OSA Integrated Photonics Research, Silicon and Nano Photonics (IPR) conference*, July 24-28, 2017, New Orleans, Louisiana, USA.
12. F. S. Chowdhury, X. Ge, and W. Zhou, "Design and Fabrication of Si_3N_4 Surface-Normal Photonic Crystal Filters and Reflectors", *the 17th IEEE International Conference on Nanotechnology (IEEE NANO 2017)*, Pittsburgh, PA, July 25-28, 2017.
13. X. Ge, M. Minkov, F. Chowdhury, S. Fan, X. Li, and W. Zhou, "Enhanced Light Emission from MoS_2 in Heterostructure Photonic Crystal Cavities", *2018 IEEE Photonics Conference*, Hilton Orlando Buena Vista Palace, Oct. 1-5, 2017, Florida, USA.
14. X. Ge, M. Minkov, X. Li., S. Fan, and W. Zhou, "Low index contrast heterostructure photonic crystal cavities with high quality factors and vertical radiation coupling", *Applied Physics Letters*, 112 (14): 141105, 2018.

15. X. Ge, M. Minkov, X. Li, S. Fan, and W Zhou, “A Large Area Monolayer WS2 Laser Based on Surface-Emitting Heterostructure Photonic Crystal Cavities”, *2018 Conference on Lasers and Electro-Optics (CLEO)*, May 13-18, 2018, San Jose, CA, USA.
16. X. Ge, M. Minkov, T. Choudhury, M. Chubarov, S. Fan, J. Redwing, X. Li, W. Zhou, “Room Temperature Photonic Crystal Surface Emitting Laser with Synthesized Monolayer Tungsten Disulfide”, *26th International Semiconductor Laser Conference*, Sept 16-19, 2018, Santa Fe, NM, USA.
17. X. Ge, M. Minkov, X. Li., S. Fan, and W. Zhou, “Direct Measurement of Directional Emission from Monolayer WS2 Laser with Heterostructure Photonic Crystal Cavities”, *2018 IEEE Photonics Conference*, Sept 30-Oct 4, 2018, Reston, VA, USA.
18. X. Ge, Z. Liu, W. Zhou, “2D Material Printing for Cavity Integration”, *2018 IEEE Research and Applications of Photonics In Defense Conference*, Aug 22-24, 2018, Miramar Beach, FL, USA.
19. X. Ge, M. Minkov, X. Li., S. Fan, and W. Zhou, “Scaling Towards Efficient Monolayer WS2 Photonic Crystal Lasers”, *2018 IEEE Photonics Society Summer Topical Meeting Series*, July 9-11, 2018, Waikoloa Village, HI, USA.
20. S-C. Liu, D. Zhao, Y. Liu, H. Yang, Y. Sun, Z. Ma, C. Reuterskiöld-Hedlund, M. Hammar, and W. Zhou, “Photonic crystal bandedge membrane lasers on silicon”, *Applied Optics*, 56(31): H67-H73, 2017.
21. Y. Shuai, D, Zhao, Y. Liu, C. Stambaugh, J. Lawall, and W. Zhou, “Coupled Bilayer Photonic Crystal Slab Electro-Optic Spatial Light Modulators”, *IEEE Photonics Journal*, 9(2): 7101411, 2017.
22. L. Yuan, Q. Lin, M. Xiao, A. Dutt, and S. Fan, "Pulse shortening in an actively mode-locked laser with a frequency-doubling nonlinear mirror," *APL Photonics*, 3, 086103 (2018).
23. A. Cerjan, M. Xiao, L. Yuan, and S. Fan, "Effects of non-Hermitian perturbations on Weyl Hamiltonians with arbitrary topological charges," *Phys. Rev. B,* 97, 075128 (2018).
24. Y. Guo, M. Xiao, and S. Fan, "Topologically Protected Complete Polarization Conversion," *Phys. Rev. Lett*. 119, 167401 (2017).

Journal manuscripts in preparation

25. X. Ge, M. Minkov, X. Li., S. Fan, and W. Zhou, “Laterally confined photonic crystal surface emitting laser incorporating monolayer tungsten disulfide”, *npj 2D Materials and Applications* (In review).
26. X. Ge, M. Minkov, T. Choudhury, M. Chubarov, S. Fan, J. Redwing, X. Li, W. Zhou, “Photonic Crystal Surface Emitting Laser with Synthesized Monolayer Tungsten Disulfide”

20. References

[1] A. Cerjan and S. Fan, "Eigenvalue dynamics in the presence of nonuniform gain and loss," *Physical Review A,* vol. 94, p. 033857, 09/30/ 2016.

[2] A. Cerjan and S. Fan, "Effects of non-uniform distributions of gain and loss in photonic crystals," *New Journal of Physics,* vol. 18, p. 125007, 2016.

[3] A. Cerjan and S. Fan, "Achieving Arbitrary Control over Pairs of Polarization States Using Complex Birefringent Metamaterials," *Physical Review Letters,* vol. 118, p. 253902, 2017.

[4] V. Liu and S. Fan, "S4: A free electromagnetic solver for layered periodic structures," *Computer Physics Communications,* vol. 183, pp. 2233-2244, 2012.

[5] A. F. Oskooi, D. Roundy, M. Ibanescu, P. Bermel, J. D. Joannopoulos, and S. G. Johnson, "MEEP: A flexible free-software package for electromagnetic simulations by the FDTD method," *Computer Physics Communications,* vol. 181, pp. 687-702, 2010.

[6] C. W. Hsu, B. Zhen, J. Lee, S.-L. Chua, S. G. Johnson, J. D. Joannopoulos*, et al.*, "Observation of trapped light within the radiation continuum," *Nature,* vol. 499, pp. 188-191, 2013.

[7] B. Zhen, C. W. Hsu, L. Lu, A. D. Stone, and M. Soljačić, "Topological nature of optical bound states in the continuum," *Physical review letters,* vol. 113, p. 257401, 2014.

[8] Y. Yang, C. Peng, Y. Liang, Z. Li, and S. Noda, "Analytical perspective for bound states in the continuum in photonic crystal slabs," *Physical review letters,* vol. 113, p. 037401, 2014.

[9] M. Khan, T. Babinec, M. W. McCutcheon, P. Deotare, and M. Lončar, "Fabrication and characterization of high-quality-factor silicon nitride nanobeam cavities," *Optics letters,* vol. 36, pp. 421-423, 2011.

[10] B.-S. Song, S. Noda, T. Asano, and Y. Akahane, "Ultra-high-Q photonic double-heterostructure nanocavity," *Nature materials,* vol. 4, pp. 207-210, 2005.

[11] K. Soon-Hong, K. Se-Heon, K. Sun-Kyung, L. Yong-Hee, and K. Sung-Bock, "Small, low-loss heterogeneous photonic bandedge laser," *Optics Express,* vol. 12, p. 5356, 11/01/ 2004.

[12] G. Z. Magda, J. Pető, G. Dobrik, C. Hwang, L. P. Biró, and L. Tapasztó, "Exfoliation of large-area transition metal chalcogenide single layers," *Scientific reports,* vol. 5, 2015.

[13] S. B. Desai, S. R. Madhvapathy, M. Amani, D. Kiriya, M. Hettick, M. Tosun*, et al.*, "Gold-Mediated Exfoliation of Ultralarge Optoelectronically-Perfect Monolayers," *Advanced Materials,* vol. 28, pp. 4053-4058, 2016.

[14] M. Amani, D.-H. Lien, D. Kiriya, J. Xiao, A. Azcatl, J. Noh*, et al.*, "Near-unity photoluminescence quantum yield in MoS2," *Science,* vol. 350, pp. 1065-1068, 2015.

[15] R. Dhall, M. R. Neupane, D. Wickramaratne, M. Mecklenburg, Z. Li, C. Moore*, et al.*, "Direct Bandgap Transition in Many-Layer MoS2 by Plasma-Induced Layer Decoupling," *Advanced Materials,* vol. 27, pp. 1573-1578, 2015.

[16] M. K. Man, S. Deckoff-Jones, A. Winchester, G. Shi, G. Gupta, A. D. Mohite*, et al.*, "Protecting the properties of monolayer MoS2 on silicon based substrates with an atomically thin buffer," *Scientific reports,* vol. 6, 2016.

[17] S. Wu, S. Buckley, J.R. Schaibley, L. Feng, J. Yan, D.G. Mandrus, F. Hatami, W. Yao, J. Vučković, A. Majumdar, and X. Xu. Monolayer semiconductor nanocavity lasers with ultralow thresholds. Nature, 520(7545), pp.69-72, 2015

[18] Y. Ye, Z.J. Wong, X. Lu, X. Ni, H. Zhu, X. Chen, Y. Wang, and X. Zhang, 2015. Monolayer excitonic laser. Nature Photonics, 9(11), pp.733-737, 2015

[19] O. Salehzadeh, M. Djavid, N.H. Tran, I. Shih, and Z. Mi, Optically pumped two-dimensional MoS2 lasers operating at room-temperature. Nano Lett, 15(8), pp.5302-5306, 2015

[20] Y. Li, J. Zhang, D. Huang, H. Sun, F. Fan, J. Feng, Z. Wang, and C.Z. Ning. Room-temperature continuous-wave lasing from monolayer molybdenum ditelluride integrated with a silicon nanobeam cavity. Nature Nanotechnology, 12(10), pp.987-992, 2017